A Numerical Study of the Composite Fermi Liquid: Probing Energy Gaps and Mass Divergences near Half-Filling

A Thesis

submitted to

Indian Institute of Science Education and Research Pune
in partial fulfilment of the requirements for the
BS–MS Dual Degree Programme

by

Shashank Gangavatiker

Indian Institute of Science Education and Research Pune
Dr. Homi Bhabha Road,
Pashan, Pune 411008, INDIA.

April, 2026

Supervisor: Dr. Prashant Kumar

All rights reserved

Certificate

This is to certify that this dissertation entitled
"A Numerical Study of the Composite Fermi Liquid" towards the partial fulfilment of the BS-MS dual degree programme at the Indian Institute of Science Education and Research, Pune represents study/work carried out by **Shashank Gangavatiker** at **IIT Bombay** under the supervision of **Dr. Prashant Kumar** during the academic year **2025-2026**.

Student Signature

Supervisor Signature

Declaration

I hereby declare that the matter embodied in the report entitled **"A Numerical Study of the Composite Fermi Liquid"** are the results of the work carried out by me at the Department of **Physics, IIT Bombay**, under the supervision of **Dr. Prashant Kumar** and the same has not been submitted elsewhere for any other degree.

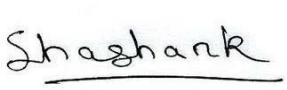

Student Signature

Supervisor Signature

Contents

List of Figures

List of Tables

Abstract

The Fractional Quantum Hall Effect (FQHE) describes the behavior of a strongly correlated 2D electron gas subject to a high perpendicular magnetic field. This results in the effective 'quenching' of kinetic energy by creating a flat-band situation where electrons are forced into discrete, massively degenerate Landau Levels. At near-zero temperatures, the electrons occupy the Lowest Landau Level (LLL) at partial filling represented by a fractional filling factor $\nu = \frac{N_e}{N_\phi}$ (for particle number N_e and LL degeneracy N_ϕ). A characteristic feature of this phenomenon is the incompressibility of the FQH phase due to the presence of robust gaps in the many-body spectrum, a consequence of the interaction-mediated lifting of degeneracy in the partially filled LLL. This problem can be formulated as an Integer Quantum Hall Effect (IQHE) of bound particles called composite fermions (CFs), where the many-body gap is replaced by the cyclotron gap separating CF Landau Levels for a reduced effective field $B^* = B(1 - 2p\nu)$.

This thesis is an attempt to utilize two commonly employed numerical techniques in condensed matter physics, Exact Diagonalization (ED) and infinite-system Density Matrix Renormalization Group (iDMRG) to examine the behavior of an incompressible FQH (Fractional Quantum Hall) phase approaching the special case of the half-filled Landau Level. In particular, we examine the scaling of gaps for fractionally charged excitations (quasi-holes and quasi-particles) above the ground state for filling fractions along the Jain sequence $\nu = \frac{p}{2p+1}$. For large p, the sequence approaches half-filling ($\nu = \frac{1}{2}$), where the vanishing effective field B^* leads to gap closure and the formation of a compressible Fermi sea of composite fermions.

Previous theoretical investigations show that the Chern-Simons field theory formulation of the half-filled FQH phase introduces renormalizations in effective mass such that it obtains a p-dependence $m^*(p)$ whose exact form depends on the nature of the underlying electron-electron interaction. By explicitly calculating the excitation gaps and probing their scaling behavior upon varying p under different interactions, the project aims to check whether the findings of numerical studies are consistent with theoretical predictions, and whether smooth variations in the interaction can capture some unique trends in scaling behavior.

Acknowledgements and Contributions

I would like to thank my supervisor, Dr. Prashant Kumar, for his guidance, encouragement, and willingness to engage in the discussions that greatly contributed to this dissertation.

I acknowledge the use of the publicly available DiagHam code package for Exact Diagonlization, which facilitated the numerical computations in this work. Furthermore, the Density Matrix Renormalization Group calculations were implemented using the code developed by Roger S.K. Mong and Michael P. Zaletel, which was adapted for the purposes of this study.

In addition, I am grateful to my parents, Rajesh and Sunita Gangavatiker, for their continuous and unwavering support throughout the period I was engaged with this work.

Generative AI Usage

The usage of Generative AI tools in the preparation of this thesis was primarily limited to the scope described in Section 4.6.1 of the 'Guidelines for Generative AI usage at IISER Pune', and accordingly no attribution is required. The specific instances where the usage extended beyond this are listed below. The GAI model used for all purposes relevant to this work was ChatGPT (OpenAI).

- GAI was occasionally used to generate keywords/phrases to aid in organizing the sentence structure for improved writing clarity.
- On one occasion, GAI was used to expand and simplify a mathematical expression utilized in result analysis. The output was appropriately edited prior to its inclusion.

Chapter 1

Introduction

1.1 The Fractional Quantum Hall Effect

The setup for the Fractional Quantum Hall Effect (FQHE) consists of 2D electrons in a high external magnetic field. The Hamiltonian for this many-body system can be expressed as a sum of the kinetic and potential energy terms:

$$H = \sum_i \frac{1}{2m} \left(\mathbf{p}_i + e\mathbf{A}(\mathbf{r}_i)\right)^2 + \sum_{i<j} V(\mathbf{r}_i - \mathbf{r}_j) \tag{1.1}$$

where the magnetic field's contribution is included in the kinetic energy by defining the gauge-invariant mechanical momentum $\Pi = \mathbf{p} + e\mathbf{A} = m\dot{\mathbf{x}}$, for vector potential $\mathbf{A}$ [1].

Following the discussion in Tong [1], the single-particle, non-interacting Hamiltonian $H = \frac{1}{2m}\left(\mathbf{p} + e\mathbf{A}\right)^2$ can be reformulated using a particular choice of gauge for the vector potential. This effectively reduces the Hamiltonian to a 1D Harmonic oscillator problem with the resultant spectrum consisting of Landau Levels with energy eigenvalues

$$E_n = \hbar\omega_B \left(n + \frac{1}{2}\right) \tag{1.2}$$

where ω_B is the cyclotron frequency $\frac{eB}{m}$, corresponding to the frequency of circular motion for a classical particle with charge e in an external field of strength B.

The Landau Levels are highly degenerate due to the freedom in choosing guiding-center positions for the semi-classical cyclotron orbits corresponding to each state. The degeneracy per level is given by $N_\phi = \frac{BA}{\Phi_0}$, where $\Phi_0 = \frac{h}{e}$ is identified as the quantum of magnetic flux. This can be interpreted as there being one state per flux quantum. The characteristic length scale is given by the magnetic length $l_b = \sqrt{\frac{\hbar c}{eB}}$, that determines the area per state $2\pi\ell_B^2 = \frac{\Phi_0}{B}$. The fraction of available states per Landau Level that are occupied is given by the filling factor $\nu = \frac{N_e}{N_\phi}$.

At partial filling corresponding to fractional ν, the many-body spectrum has massive degeneracy ($\frac{\nu N_\phi}{N_\phi}$), ensuring that no configuration is energetically favored prior to interactions. In addition, the kinetic energies of the electrons are effectively 'frozen' due to the separation between the LL transition cost and the interaction energy scale $\hbar\omega_c >> \frac{e^2}{l_b}$. Since Landau Level transitions are forbidden, the system is confined to the Lowest Landau Level (LLL) which can be represented by projecting the many-body Hamiltonian as

$$H_{\text{LLL}} = \mathscr{P}_{\text{LLL}} \left(\sum_{i<j} V(\mathbf{r}_i - \mathbf{r}_j) \right) \tag{1.3}$$

This makes the system consist of interacting electrons in a flat band, resulting in a strongly correlated phase where the ground state is exclusively determined by electron-electron interactions.

The choice of gauge is based on the geometry of the system. For cylindrical geometry we use the Landau gauge $\mathbf{A} = (0, Bx, 0)$ which removes the y-dependence of the vector potential ensuring translational invariance along the cylinder's circumference. Alternatively the symmetric gauge $\mathbf{A} = \frac{B}{2}(-y, x, 0)$ is used in rotationally invariant systems, making it a natural choice for disc and sphere geometries. Further analysis of FQHE states on the sphere and the cylinder for Exact Diagonalization and iDMRG, respectively, will be elaborated on in Chapter 2.

1.2 The Laughlin State and Charged Excitations

The lowest-energy configuration is given by the many-body state, which minimizes repulsion in the LLL. This principle is encapsulated by the trial wavefunction given by Laughlin [2]

$$\Psi_m = \prod_{i<j} (z_i - z_j)^m e^{-\sum_i |z_i|^2 / 4\ell_B^2} \tag{1.4}$$

where filling fraction $\nu = \frac{1}{m}$. Fermionic antisymmetry is imposed by restricting m to odd values. The Jastrow factor $\prod_{i<j}(z_i - z_j)^m$ includes the correlations between pairs of particles by suppressing the wavefunction as the particles approach each other. The degree of suppression given by the order of the zero in the Jastrow factor m, which is the relative angular momentum quantum number. This factor eliminates all states that contain two-particle configurations with relative angular momentum $< m$, ensuring that the particles avoid each other due to stronger suppression of short-distance particle configurations.

Following the treatment in Tong [1], the Laughlin wavefunction represents the densest state which manages to minimize repulsive interactions for a particular filling fraction ν. Thus, any deviation in density due to the addition/removal of particles costs a finite energy by forcing particles into more repulsive configurations, resulting in a gapped many-body spectrum above the ground state. This results in the incompressibility of the Laughlin phase as a direct consequence

of the energy penalty for fluctuations above the ground state.

The presence of the gap suppresses the long-wavelength density modes that correspond to global deformations of the Laughlin fluid. Thus, the lowest energy excitations above the ground state consist of localized changes in electron density, with local charge excess and deficit corresponding to the quasi-particle and quasi-hole excitations respectively. The wavefunction for quasi-hole at position η is

$$\Psi_{\text{qh}}(\eta) = \prod_i (z_i - \eta)\,\Psi_m \tag{1.5}$$

which suppresses the probability of finding an electron near the quasi-hole by introducing an extra zero at position η, thus creating a 'hole' in the electron fluid.

In the Laughlin wavefunction, the maximum polynomial degree for each particle coordinate z_i determines the maximum angular momentum per particle $m_{max} = m(N-1)$, which defines the spatial extent of the state. This is quantified by the radius of the FQH droplet $r \sim \sqrt{2m_{max}}\,\ell_B$, which can be used to write the area of the droplet in terms of the number of flux quanta $A = 2\pi\ell_B^2 N_\phi$. The quasi-hole modification to this state introduces the prefactor $\prod_i (z_i - \eta)$ which increases the degree for each z_i by one. This is mathematically equivalent to adding one extra flux quantum to the system $N_\phi \to N_\phi + 1$.

Since adding flux increases the number of available single-particle states with respect to particle number, maintaining the same particle density by fixing ν would require increasing the particle number to $N_e' = \nu(N_\phi + 1)$. Since these ν additional electrons are not added, the quasi-hole state obtains a fractional charge deficit of $\nu e = \frac{e}{m}$. This corresponds to a collective redistribution of the Laughlin fluid where each particle is slightly displaced so that the charge deficit is localized near the excitation.

Similarly, quasi-particles are excitations over the Laughlin phase carrying fractional charge $-\frac{e}{m}$, corresponding to local excess in charge density. This requires decreasing the relative angular momentum for some pairs of particles, which is achieved in the wavefunction by differentiating with respect to particle coordinate z_i to reduce the polynomial degree

$$\psi_{\text{qp}}(z,\eta) = \left[\prod_{i=1}^{N}\left(2\ell_B^2\frac{\partial}{\partial z_i} - \bar{\eta}\right)\prod_{k<l}(z_k - z_l)^m\right] e^{-\sum_{i=1}^{N}|z_i|^2/4\ell_B^2} \tag{1.6}$$

The quasi-particle and quasi-hole excitations are typically created as QP-QH pairs to maintain charge neutrality. The charged excitation gap for ground state energy E_0 is thus defined as

$$\Delta \sim E_{\text{qe}} + E_{\text{qh}} - 2E_0 \tag{1.7}$$

where $\Delta > 0$ for the incompressible FQH phase. Thus, a finite gap value obtained from numerics confirms the stability of the Laughlin ansatz.

1.3 Interaction Hamiltonian and Pseudopotentials

The LLL wavefunctions are highly constrained as they are required to be analytic functions of particle coordinates $f(z)$, as seen in the Laughlin ansatz. This reduces the range of allowed particle configurations in the many-body state, resulting in the need for a more convenient basis to represent the interaction beyond the real-space form $V(|r_i - r_j|)$.

Following the analysis in Tong [1], any two-particle LLL state can be decomposed into relative and centre-of-mass parts

$$\psi(z_1, z_2) = (z_1 - z_2)^m (z_1 + z_2)^n \, e^{-(|z_1|^2 + |z_2|^2)/4\ell_B^2} \tag{1.8}$$

where integer m is the relative angular momentum of the two-particle state. Since the interaction depends only on the relative coordinate, it is diagonal under the choice of a two-particle basis with definite m, labeled $\mid \psi_m \rangle$. Thus, the interaction can be expressed in terms of the energy cost for pairs of particles having relative angular momentum m. This energy cost is defined as the Haldane Pseudopotential V_m and is written as the matrix element

$$V_m = \frac{\langle \psi_m \mid V(r) \mid \psi_m \rangle}{\langle \psi_m \mid \psi_m \rangle} \tag{1.9}$$

The value of m also quantifies the degree of 'closeness' between the two particles in the state $\mid \psi_m \rangle$ as it relates to the spatial extent of the two-body wavefunction. Mathematically, the probability density $|\psi_m|^2$ peaks at radius $r \approx \sqrt{2m}\,\ell_B$. Thus, a higher m corresponds to a greater separation between the particles with a lower energy cost V_m, and vice-versa. For fermionic systems, even values of m are excluded by antisymmetry with the resulting pseudopotentials $V_1 > V_3 > V_5 > ...$ etc. In second quantization, the interaction Hamiltonian is expressed by summing over the pseudopotentials as

$$\hat{H}_{\text{int}} = \sum_{i<j} \sum_m V_m \hat{P}_{ij}(m) \tag{1.10}$$

where $\hat{P}_{ij}(m)$ is the projector operator that only selects pairs of particles i and j that have relative angular momentum m.

Since the Laughlin wavefunction eliminates all two-particle configurations having $m' < m$, it avoids interaction channels with the highest energy costs, making it energetically favorable. In particular, the Laughlin state is the exact ground state for the V_1 interaction $H = V_1 P_1$ or more general truncated pseudopotential interactions, as demonstrated by Haldane and Rezayi [3].

For planar geometry, the pseudopotentials can be written in terms of the Fourier transform of the interaction in momentum space $V(q)$ and the corresponding Laguerre polynomials L_m as

noted in [4]. The planar pseudopotentials are expressed as

$$V_m = \int_0^\infty dq\, q V(q) L_m(q^2\ell_B^2)\, e^{-q^2\ell_B^2} \tag{1.11}$$

which is obtained by projecting the interaction to the LLL. Pseudopotentials specific to the spherical and cylindrical geometry, which will be used in numerical calculations, will be discussed in Chapter 2.

1.4 Composite Fermions and Effective Field Theories

The Laughlin wavefunction is successful at approximating states with filling fractions of the form $\nu = \frac{1}{m}$. However, many deviations from this standard are observed in FQH experiments with filling fractions taking values such as $\frac{2}{5}, \frac{3}{7}, \frac{4}{9}$ etc. Along with the Laughlin state, this results in the observed hierarchy of states represented as $\nu = \frac{n}{2pn+1}$. This hierarchy can be explained using the Composite Fermion (CF) theory developed by Jain [5], which maps the problem of the strongly correlated electron fluid in the LLL to weakly interacting particles called 'composite fermions' in a reduced effective magnetic field B^*. A brief description of the composite fermion theory following the discussion in Vestigian [6] is provided in this section.

Mathematically, the CF mapping is implemented by defining the unitary transformation

$$U = \exp\left(-i\sum_{i<j}\frac{\theta}{\pi}\alpha_{ij}\right) \tag{1.12}$$

where $\alpha_{ij} = \arg(r_i - r_j)$ is the angle of the vector connecting particles i and j, and the parameter θ controls the phase attached per pair of particles. The Hamiltonian transforms under U as $H' = U^{-1}HU$ with the momentum operator transforming as

$$U^{-1}\left(\mathbf{p}_i - \frac{e}{c}\mathbf{A}\right)U = \mathbf{p}_i - \frac{e}{c}\mathbf{A} - \frac{\hbar\theta}{\pi}\sum_{j\neq i}\nabla\alpha_{ij} \tag{1.13}$$

where the original kinetic momentum term is left intact after the transformation, along with an added extra factor $-\frac{\hbar\theta}{\pi}\sum_{j\neq i}\nabla\alpha_{ij}$. This is used to define the statistical gauge field

$$\mathbf{a}(\mathbf{r}_i) = \frac{\phi_0\theta}{2\pi^2}\sum_{j\neq i}\nabla\alpha_{ij} \tag{1.14}$$

The transformed Hamiltonian can now be written as

$$H' = \sum_i \frac{1}{2m}\left[\mathbf{p}_i - \frac{e}{c}\mathbf{A} - \frac{e}{c}\mathbf{a}\right]^2 + \sum_{i<j}V(\mathbf{r}_i - \mathbf{r}_j) \tag{1.15}$$

where $\mathbf{a}(\mathbf{r}_i)$ represents the new vector potential experienced by a particle at position i due to all

other particles in the system, in addition to vector potential due to the external magnetic field $\mathbf{A}(\mathbf{r}_i)$. Taking the curl to obtain the effective magnetic field corresponding to the statistical gauge field, we obtain

$$\nabla \times \mathbf{a}(\mathbf{r}) = \frac{\theta \Phi_0}{\pi} \rho(\mathbf{r}) \tag{1.16}$$

where $\rho(\mathbf{r}) = \sum_j \delta(\mathbf{r} - \mathbf{r}_j)$ is the particle density. Thus, magnetic flux exists only in regions of non-zero particle density, with a magnetic flux of magnitude $\theta\Phi_0$ attached per particle.

On swapping the positions of particles r_i and r_j the angle between the vector connecting them and the x-axis transforms as $\alpha_{ji} \to \alpha_{ij} + \pi$. Thus, the unitary operator U gains phase $e^{-\frac{i\theta}{\pi}}$ on exchanging particles. Starting with an antisymmetric wavefunction ψ, the transformed wavefunction $\phi = U^{-1}\psi$ remains antisymmetric under particle exchange only if this additional phase in U is equal to one. Thus, for fermionic CF mapping we define the phase $\theta = 2p\pi$ for integer-valued p. Equation (1.16) now becomes $\nabla \times \mathbf{a}(\mathbf{r}) = 2p\Phi_0\rho(\mathbf{r})$, where the effective field is interpreted as arising from attaching an even number of flux quanta per particle.

This allows the problem to be redefined in terms of composite fermions, where each CF is a bound system consisting of an electron attached to $2p$ flux quanta. Under mean-field approximation, we replace $\rho(\mathbf{r})$ with the average particle density $n = \langle \rho(\mathbf{r}) \rangle$ while ignoring fluctuations over the mean field $\delta\rho$. Since the total magnetic field felt by the particles is $\mathbf{B} = \nabla \times (\mathbf{A} + \mathbf{a})$, the resulting effective magnetic field felt by the composite fermions is $B^* = B - 2p\Phi_0 n$, obtained by removing the contribution from $\mathbf{a}$. For electron filling, we have $\nu = \frac{n\Phi_0}{B}$. Substituting $n\Phi_0$ into the expression for B^*,we get $B^* = B(1 - 2p\nu)$ and CF filling fraction

$$\nu^* = \frac{n\Phi_0}{B^*} = \frac{\nu B}{B(1-2p\nu)} = \frac{\nu}{1-2p\nu} \tag{1.17}$$

Inverting this relation, we can write electron filling in terms of CF filling as

$$\nu = \frac{\nu^*}{1+2p\nu^*} \tag{1.18}$$

If we restrict CFs to occupy Landau Levels at integer filling $\nu^* = n \in Z$, we obtain the filling fraction for the hierarchy of states as $\nu = \frac{p}{2pn+1}$, which for $n = 1$ reproduces the observed Jain states $\frac{1}{3}, \frac{2}{5}, \frac{3}{7}, \frac{4}{9}$ etc. Thus, the FQHE for electrons can be mapped to an equivalent problem of the IQHE (Integer Quantum Hall Effect) for composite fermions.

1.5 The Half-Filled Landau Level

As we increase the number of filled CF Landau Levels p for the Jain states, we approach the special case of half-filling ($\nu = \frac{1}{2}$). Following the expression for the reduced effective field stated in section 1.4, the magnetic field is exactly canceled by the magnetic flux 'absorbed' by the composite fermions, and the CFs experience a vanishing effective field $B^* = 0$.

Since the gaps in the CF spectrum are related to the cyclotron frequency as $\Delta = \frac{\hbar\omega_c}{m^*}$ (where m^* is the effective mass of the CF), the quantization of LL is no longer supported at half-filling, leading to the closure of the gap. Thus, the state loses compressibility and forms a Fermi sea of CFs, also referred to as the Compressible Fermi Liquid (CFL) [1].

Under the mean-field approximation where fluctuations in particle density and the corresponding gauge field **a** are ignored, the CFs are non-interacting with a constant effective mass m^*. As the system approaches half-filling for large p, the effective magnetic field scales as $B^* = \frac{B}{2p+1}$ (setting $n = 1$), giving a gap that scales linearly with $\frac{1}{2p+1}$. However, a deeper analysis of the half-filled Landau Level by Halperin, Lee and Read (HLR) [7] shows that when the mean field approximation is relaxed, the corresponding fluctuations in the gauge field mediates interactions between the composite fermions. This results in effective mass renormalization, due to which it gains a p dependence $m^*(p)$. The exact nature of this p dependence arises from the form of the underlying electronic interaction in Fourier space, $V(q)$ [7].

This project attempts to investigate the behavior of FQH states approaching the CFL phase, and to verify if the findings of numerical techniques probing the half-filled case are consistent with theoretical predictions, and whether they can provide insights into the nature of the CFL.

Chapter 2

Methods

2.1 Fractional Quantum Hall systems on the Sphere

One of the standard techniques in FQH numerics is to map the planar 2D electron gas to the surface of a sphere. This construction, provided by Haldane [8], is used extensively in exact diagonalization studies, as it removes boundary conditions and preserves rotational symmetry. This is achieved through a stereographic projection, which creates a one-to-one mapping between points on an infinite 2D plane and points on the sphere. This allows us to shift the problem to a more feasible, finite-sized system. Following the discussion in [8], a brief description of the salient features of this setup is provided in this section.

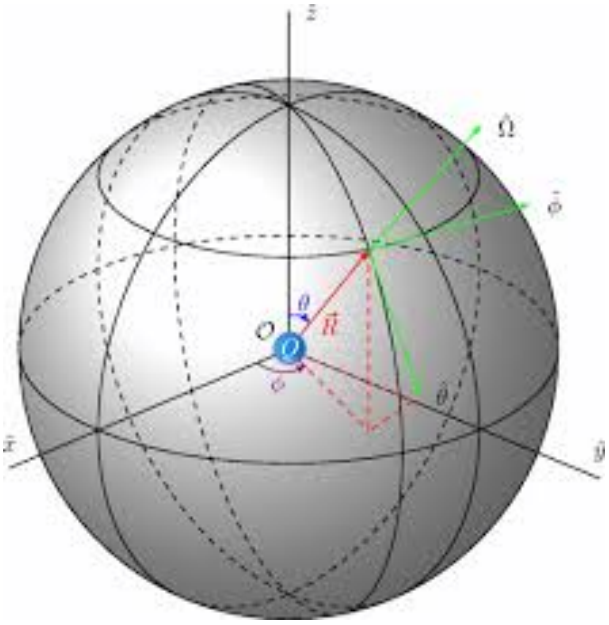

Figure 2.1: Haldane sphere schematic. Reproduced from Ref. [9] Copyright © American Physical Society.

The Haldane sphere setup consists of N electrons restricted to the surface of a sphere of radius R. A magnetic monopole of strength g placed at the center generates the field in the

radial direction $\hat{\Omega}$

$$\vec{B} = \frac{g}{R^2}\hat{\Omega} \tag{2.1}$$

Taking into consideration the uniform magnetic field normal to the surface of the sphere, the total flux is simply $\Phi = B \cdot 4\pi R^2 = 4\pi g$, thus making it depend only on the monopole charge magnitude. According to the flux quantization condition given by Dirac, the total flux should be an integer multiple of the flux quantum, $4\pi g = N_\phi \Phi_0$. Here, N_ϕ is defined within the context of the quantum hall problem as $2Q$, where Q is a dimensionless parameter regarded as the 'monopole strength' which is related to the actual physical charge as $Q = \frac{eg}{\hbar}$. The total flux is more generally written in units of flux quanta as $2Q$.

As in the 2D case, the single-particle Hamiltonian for a spherical system can be written by incorporating the effect of the radial field within the mechanical momentum Π as $H = \frac{\vec{\Pi}^2}{2m}$, where $\vec{\Pi} = \vec{p} + e\vec{A}$. Since the natural choice of quantum numbers on the sphere is angular momentum, the Hamiltonian can be rewritten in terms of the gauge-invariant mechanical angular momentum $\vec{\Lambda} = \vec{r} \times \vec{\Pi}$ as

$$H = \frac{\Lambda^2}{2mR^2} \tag{2.2}$$

where the magnitude $\Lambda^2 = r^2\Pi^2 - (\vec{r} \cdot \vec{\Pi})$. For fixed radius, $r = R$ and the dot product goes to zero as the electron motion is tangential to radial direction. Although $\vec{\Lambda}$ is analogous to the particle angular momentum, it does not follow the expected angular momentum algebra and hence cannot be used to generate rotations of the system. For this purpose, the total angular momentum $\vec{L}$ is introduced as

$$\vec{L} = \vec{\Lambda} - Q\hbar\hat{\Omega} \tag{2.3}$$

Where the components of $\vec{L}$ follow the required SU(2) commutation relations $[L_i, L_j] = i\hbar\varepsilon_{ijk}L_k$. The Hamiltonian can be rewritten in terms of $\vec{L}$ as

$$H = \frac{1}{2mR^2}\left(L^2 - Q^2\hbar^2\right) \tag{2.4}$$

Thus, the eigenstates of the system are angular momentum eigenstates with energies E_l obtained by substituting $L^2 = \hbar^2 l(l+1)$

$$E_l = \frac{\hbar^2}{2mR^2}\left[l(l+1) - Q^2\right] \tag{2.5}$$

Since the Hamiltonian is the square of an operator, we require $l(l+1) > Q^2$. Thus, the smallest allowed value of l is Q and we can define $l = Q + n$ with $n = 0, 1, 2....$ Thus, the index n labels the Landau Levels with the energies

$$E_n = \frac{\hbar^2}{2mR^2}\left[n(2Q + n + 1)\right] \tag{2.6}$$

For the LLL, $l = Q$ and the degeneracy is thus $N_\phi + 1$, where the extra orbital compared to the

planar degeneracy N_ϕ comes from the curvature of the sphere. The orbitals are labeled by the L_z component $m = -Q, -Q+1, ...Q$.

From expression (2.6), we can calculate the energy gap

$$\Delta E = E_{n+1} - E_n = \frac{\hbar^2}{mR^2}(Q+n+1) \tag{2.7}$$

On writing Q in terms of the magnetic field B as $Q = \frac{eBR^2}{\hbar}$ and substituting the cyclotron frequency $\omega_c = \frac{eB}{m}$, we obtain

$$\Delta E = \hbar\omega_c + \frac{\hbar^2}{mR^2}(n+1) \tag{2.8}$$

Where the second term in the sum is the correction due to the finite curvature of the sphere. As $R \to \infty$ in the thermodynamic limit, the gap reduces to the planar LL spacing.

Following [8], the wavefunctions on the Haldane sphere are the monopole harmonics $Y_{Qlm}(\theta, \phi)$, which are nontrivial functions of the angular coordinates θ and ϕ. The form of the wavefunction is simplified by switching to the spinor coordinates $u = \cos(\frac{\theta}{2})e^{i\phi/2}$ and $v = \sin(\frac{\theta}{2})e^{-i\phi/2}$ where $|u|^2 + |v|^2 = 1$. Thus, each point on the sphere can be represented as a normalized spinor, and rotations of the sphere can be mapped to SU(2) transformations of the two-component spinor.

Since the LLL monopole harmonics$|Q,m\rangle$ form the spin-Q representation for the SU(2) rotation group, the natural basis to represent the wavefunctions is $u^{Q+m}v^{Q-m}$. The normalized wavefunctions can be written as

$$\psi_m(u,v) = \sqrt{\binom{2Q}{Q+m}}\, u^{Q+m}v^{Q-m} \tag{2.9}$$

for m ranging from $-Q$ to Q. The many-body wavefunction can be constructed as antisymmetric Slater determinants involving these single-particle orbitals.

As seen in equation (2.9), every LLL wavefunction is a homogenous polynomial with degree $2Q$. On the sphere, the $(z_i - z_j)$ factor is replaced with the rotationally invariant combination $(u_i v_j - u_j v_i)$ to obtain the Laughlin wavefunction

$$\Psi = \prod_{i<j}(u_i v_j - u_j v_i)^q \tag{2.10}$$

where for each particle i, the wavefunction contains the factor $(u_i v_j - u_j v_i)^q$ for all $j \neq i$. Thus, for a system of N_e particles, the number of such factors is $(N_e - 1)$, leading to a total polynomial degree of $q(N_e - 1)$ per particle. However, since the many-body state is composed of homogeneous single-particle wavefunctions, equation (2.9) requires that the Laughlin wavefunction has a degree of $2Q = N_\phi$ for each particle coordinate, giving us the relation $N_\phi = q(N-1)$.

More generally, the flux-particle relation is written as

$$N_\phi = \nu^{-1} N_e - S \tag{2.11}$$

where the shift S is a topological quantum number that arises from the curvature of the sphere. For the Laughlin state, the filling fraction $\nu = \frac{1}{3}$ and $S = Q$.

Due to rotational symmetry, the Hamiltonian commutes with the angular momentum operators L^2 and L_z for the many-body system, and the eigenstates can be labeled as $|L,M\rangle$. The Laughlin state is also rotationally invariant as it is the unique ground state describing a homogeneous quantum hall phase. Since there is no preferred direction due to the uniform electron density, the state is rotationally invariant and is identified as the singlet $L = 0$. On the other hand, quasi-hole and quasi-particle wavefunctions have angular momentum $L = \frac{N_e}{2}$ for number of particles N_e, corresponding to a degeneracy of $N_e + 1$.

The interaction on the sphere can be described conveniently using the pseudopotential formulation introduced in chapter 1. Following the derivation of Wooten [10], the key details leading to the expression for spherical pseudopotentials implemented in this study, are outlined here. The many-body interaction Hamiltonian $H = \sum_{i<j} V(|\mathbf{r}_i - \mathbf{r}_j|)$ can be written in second quantization in terms of the two-body matrix elements involving the monopole harmonics $|Q,l,m\rangle$ as

$$\begin{aligned} &\langle Q,l_1',m_1';\, Q,l_2',m_2' \mid \hat{V} \mid Q,l_1,m_1;\, Q,l_2,m_2\rangle \\ &= \int Y^*_{Ql_1'm_1'}(\Omega_1)\, Y^*_{Ql_2'm_2'}(\Omega_2)\, V(r_{12})\, Y_{Ql_1m_1}(\Omega_1)\, Y_{Ql_2m_2}(\Omega_2)\, d\Omega_1\, d\Omega_2 \end{aligned} \tag{2.12}$$

where the states are labeled by the single-particle quantum numbers and the interaction depends only on relative separation. The matrix element is a non-trivial expression involving integrals over the angular coordinates for both particles Ω_1 and Ω_2. This can be simplified by exploiting the rotational invariance of the Hamiltonian by rewriting the matrix element in the coupled basis $|L,M\rangle$ that corresponds to the pair angular momentum $\vec{L_{12}} = \vec{L_1} + \vec{L_2}$.

Thus, we can expand the uncoupled two-body state labeled by the angular momentum quantum numbers for the individual particles in terms of the coupled basis

$$|l_1m_1;l_2m_2\rangle = \sum_{L,M} |l_1l_2;LM\rangle\langle l_1l_2;LM \mid l_1m_1;l_2m_2\rangle \tag{2.13}$$

where $\langle l_1l_2;LM|l_1m_1;l_2m_2\rangle$ are the Clebsch-Gordon coefficients for monopole harmonics, obtained from the standard angular momentum addition rules (Edmonds [11]).The monopole charge Q is omitted here for brevity.

The addition rules provide the allowed values $L = |l_1 - l_2|.....l_1 + l_2$, which for electrons in the LLL ($l_1 = l_2 = Q$) gives us $L = 0,1,2...2Q$.

Substituting the coupled basis expansion into the matrix element:

$$\langle l_1' m_1'; l_2' m_2' | \hat{V} | l_1 m_1; l_2 m_2 \rangle = \sum_{L',M',L,M} \langle l_1' m_1'; l_2' m_2' | l_1' l_2'; L' M' \rangle \times \langle l_1' l_2'; L' M' | \hat{V} | l_1 l_2; LM \rangle \langle l_1 l_2; LM | l_1 m_1; l_2 m_2 \rangle. \tag{2.14}$$

Since the interaction is rotationally invariant, $[\hat{V}, L^2] = [\hat{V}, L_z] = 0$ and the matrix elements $\langle l_1' l_2'; L' M' | \hat{V} | l_1 l_2; LM \rangle$ are diagonal in L and M:

$$\langle l_1' l_2'; L' M' | V | l_1 l_2; LM \rangle = \delta_{LL'} \delta_{MM'} V(L) \tag{2.15}$$

Where $V(L)$ is the pseudopotential, defined on the sphere as the energy cost for two-body states with definite pair angular momentum L. The pseudopotentials can also be expressed in terms of relative angular momentum as in the planar case using the relation $V_m = V(L = 2l - m)$. Like m, L quantifies the degree of separation between the two particles. This can be verified qualitatively by considering the magnitude for a general pair angular momentum $\vec{L_{12}} = \vec{L_1} + \vec{L_2}$:

$$L_{12}^2 = l_1^2 + l_2^2 + 2\,\vec{l_1} \cdot \vec{l_2} \tag{2.16}$$

Since the magnitude is determined by the sign of $\vec{l_1} \cdot \vec{l_2}$, large values of L corresponds to parallel configuration of the vectors l_1 and l_2,whereas smaller values corresponds to the anti-parallel configuration. On the Haldane sphere, the single-particle angular momentum directions correspond to the guiding-center positions for the Landau orbitals. Thus when $\vec{l_1}$ and $\vec{l_2}$ are aligned, they represent particles lying closer together on the sphere, whereas opposing angular momenta correspond to particles lying far apart.

Since the interaction $\hat{V}$ depends only on the relative separation r_{12}, it can be expressed on the sphere in terms of the angle between the particles $cos\theta_{12} = \hat{r_1} \cdot \hat{r_2}$. The interaction is expanded using the Legendre polynomial decomposition:

$$V(r_{12}) = \sum_k V_k P_k(\cos\theta_{12}) \tag{2.17}$$

The Legendre polynomials can be expressed as products of single-particle monopole harmonics using the spherical harmonic addition theorem:

$$P_k(\cos\theta_{12}) = \frac{4\pi}{2k+1} \sum_m Y_{km}^*(\Omega_1)\, Y_{km}(\Omega_2) \tag{2.18}$$

Thus, the matrix element in the uncoupled basis (2.14) reduces to a product of separate integrals over single-particle angular coordinates Ω_1 and Ω_2. This makes it possible to evaluate the matrix element using standard angular momentum algebra. The resultant integrals over the monopole harmonics can be evaluated using the identities derived by Wu and Yang [12].

The final expression for the pseudopotentials $V(L)$ obtained after evaluating the matrix elements (2.14) and expanding them in the pair angular momentum basis $|L,M\rangle$ is given by:

$$V(L) = \frac{1}{\sqrt{Q}} \sum_{k=0}^{2l} V_k (-1)^{2Q+L} (2l+1)^2 \begin{Bmatrix} L & l & l \\ k & l & l \end{Bmatrix} \begin{pmatrix} l & k & l \\ -Q & 0 & Q \end{pmatrix}^2 \tag{2.19}$$

as stated in [10], where k labels the angular momentum channel arising from the Legendre expansion of the interaction potential. The Wigner $3j$ symbols (denoted by parentheses) come from evaluating integrals over monopole harmonics involving the coupling of three angular momenta, whereas the $6j$ symbols (denoted by curly brackets) arise when expressing the interaction in definite pair angular momentum basis.

The pseudopotentials $V(L)$ were computed explicitly using Python by expressing the real-space interaction $V(r)$ in polar form where the inter-electron separation was obtained using the chord-distance $r(\theta) = 2R\sin\frac{\theta}{2}$. The Wigner symbols were evaluated using the symbolic algebra package Sympy, and the values for the resultant coulomb pseudopotentials were verified by comparing them with known values obtained from the DiagHam code package [13].

2.2 Exact Diagonalization and Finite-Size Corrections

The interaction Hamiltonian is diagonalized in the many-body Hilbert space for particles in the LLL, to obtain the ground state energy and the charged excitation gaps corresponding to quasi-holes and quasi-particles. For LL degeneracy $N_\phi + 1$ on the sphere, the dimension of the Hilbert space for N_e particles is thus:

$$\dim(\mathscr{H}) = \binom{N_\phi + 1}{N_e} \tag{2.20}$$

which scales exponentially with system size, limiting ED to small particle numbers. The many-body basis states are Slater determinants involving the single-particle states labeled by the L_z component $m = -l...l$, which can be written in the occupation number representation as $|n_{-l}, n_{-l+1}...n_l\rangle$ where $n_m = 0$ or 1 for fermions. The Hamiltonian in second quantization is

$$H = \frac{1}{2} \sum_{m_1 m_2 m_3 m_4} V_{m_1 m_2 m_3 m_4} c^\dagger_{m_1} c^\dagger_{m_2} c_{m_4} c_{m_3} \tag{2.21}$$

where $V_{m_1 m_2 m_3 m_4}$ is the two-body matrix element obtained from the pseudopotential $V(L)$. The Hamiltonian is represented as a matrix in the occupation number basis.

The rotational invariance of the system results in a sparse Hamiltonian matrix. This is because the occupation basis has a definite total $L_z = \sum_i m$ (where i is summed over the filled orbitals), and since $[H, L_z] = 0$ the Hamiltonian does not connect basis states with different total L_z. Thus the basis states are grouped by L_z, resulting in a block-diagonal form for the

Hamiltonian, with each block corresponding to a fixed L_z sector. This allows the Hamiltonian to be diagonalized within each sector, significantly lowering the computational cost. ED was implemented using the DiagHam code package [13], which employs iterative algorithms like Lanczos to converge towards the ground state.

The excitation energies and gaps were calculated using the method outlined in Morf et al. [4]. For quasi-like excitations, the flux-particle relation (2.11) for excitations over the ground state at filling fraction $\nu = \frac{p}{2p+1}$ is modified by adding (removing) the term $\frac{1}{p}$, to account for the extra or missing flux for quasi-hole (QH) and quasi-particle (QP) respectively. Thus, the modified flux-particle relation becomes

$$N_\phi = \nu^{-1} N_e - S \pm \frac{1}{p} \tag{2.22}$$

Since we require an integer number of pseudopotentials labeled by $m = 2Q - L_{12}$ and the pair angular momentum L_{12} takes integral values from 0 to $2l$, it follows that the total flux $N_\phi = 2Q$ is required to be integer-valued. However, the flux mismatch between the ground state and the excited states due to the additional factor $\pm\frac{1}{p}$ results in a discrepancy in the allowed particle numbers for which the flux is integer valued for the ground and the excited states. This was addressed by calculating energies at different particle numbers for the ground, quasi-hole and quasi-particle states and then carefully interpolating/extrapolating the excited state energies to match the ground state particle numbers. The energy values at the same N_e were then subtracted in accordance with the gap definition (1.7).

ν	GS (N_e)	QP (N_e)	QH (N_e)
$1/3$	6, 8, 10, 12	6, 8, 10, 12	6, 8, 10, 12
$2/5$	6, 8, 10, 12, 14	7, 9, 11, 13	7, 9, 11, 13
$3/7$	6, 9, 12, 15	7, 10, 13, 16	5, 8, 11, 14
$4/9$	8, 12, 16	9, 13, 17	7, 11, 15

Table 2.1: Particle numbers N_e for GS, QP and QH states used in the exact diagonalization calculations for various filling fractions

The excited state energy gaps (Δ_{qp} and Δ_{qh}) obtained from ED were plotted against $1/N_e$, with the gap values in the thermodynamic limit estimated from extrapolating the linear fits. The total charged excitation gap ($\Delta = \Delta_{qh} + \Delta_{qp}$) was obtained by summing the two linear fits.

The sphere radius R is related to the total flux as $R = \sqrt{Q} l_b$ for magnetic length l_b, and the energies are usually reported in units of magnetic length $\frac{e^2}{l_b}$. At fixed filling ν, the areal electron density on the sphere should remain constant as the system size N_e is varied, so that the change in size does not reflect in the per-particle ground state energy. This ensures that we compare the same physical system at different N_e. However, the density of electrons on the sphere obtains an artificial size dependence as noted by Morf et al [14]. Substituting $R = \sqrt{Q} l_b$ and using the

flux-particle relation (2.11), the electron density can be written as:

$$\rho = \frac{N_e}{4\pi R^2} = \frac{\nu}{2\pi l_b^2}\frac{N_e}{N_e - \nu S} \tag{2.23}$$

for shift S. This N_e-dependence of the density ρ is rectified by defining the modified magnetic length

$$l_0 = \sqrt{\frac{2Q\nu}{N_e}} l_b \tag{2.24}$$

and expressing all energies in units of $\frac{e^2}{l_0}$. The density then reduces to the N_e-independent expression $\rho = \frac{\nu}{2\pi l_0^2}$, where the size-dependence is absorbed by l_0.

Following Morf et al. [4], the excitation energies receive contributions from the non-uniform charge distribution that arises when a quasi-hole or quasi-particle with charge of magnitude $q = \frac{1}{2p+1}$ (for $e = 1$)is localized at a point on the sphere. This shows up as a finite-size effect that vanishes in the thermodynamic limit, and has to be subtracted for accurate gap extrapolation. In the ground state, the charge on the sphere due to the electron density (ρ_e) is balanced by a uniform positively charged background density (ρ_b) to maintain net charge neutrality (Jellium model), so that the system has a well-defined energy under the thermodynamic limit. On locally introducing additional charge $\pm q$, the system maintains neutrality by redistributing the charge excess/deficit as a compensating background charge $\mp q$ over the whole sphere, resulting in a uniform change in background density of magnitude $\delta\rho_b = \frac{q}{4\pi R^2}$. For a charge q localized around a point specified by unit vector direction $\hat{\Omega}_0$, this correction A_q can be calculated analytically as:

$$A_q = q\int_{\Omega} \delta\rho_b(\Omega) V(r(\Omega,\Omega_0))\, d\Omega + \frac{1}{2}\int_{\Omega}\int_{\Omega'} \delta\rho_b(\Omega) V(r(\Omega,\Omega'))\delta\rho_b(\Omega')\, d\Omega d\Omega' \tag{2.25}$$

where the integrals are evaluated over the angular coordinates Ω and Ω'. The first term in the sum is the change in energy due to the interaction of the charge with the compensating change in background density, whereas the second term is the self-energy corresponding to the uniform density fluctuation $\delta\rho = \frac{-q}{4\pi R^2}$.

For the Coulomb interaction $V(r) = \frac{1}{r}$, it follows from Gauss's law that the potential generated by the uniform charge distribution $\delta\rho$ has the same value $\frac{q}{R}$ at every point on the sphere. This simplifies the integrals in (2.25) to:

$$A_q = q\left(\frac{-q}{R}\right) + \frac{1}{2}\left(\frac{q^2}{R}\right) = \frac{-q^2}{2R} \tag{2.26}$$

In energy units of $\frac{e^2}{l_0}$, this expression reduces to

$$A_q = -q^2\sqrt{\frac{\nu}{2N_e}} \tag{2.27}$$

Following the treatment of Balram et al. [15], we have to additionally include contributions to the total energy due to interactions of the electrons with the uniform jellium background $\rho_b(\Omega)$ denoted by E_{eb} and the background-background interaction energy denoted byE_{bb}. Thus, the total background correction to be added to the energy obtained from ED is given by the expression:

$$E_{eb}+E_{bb}=-\sum_{i=1}^{N_e}\left(\int_{\Omega}\rho_b(\Omega)V(r(\Omega,\Omega_i))\,d\Omega\right)+\frac{1}{2}\int_{\Omega}\int_{\Omega'}\rho_b(\Omega)V(r(\Omega,\Omega'))\rho_b(\Omega')\,d\Omega d\Omega' \tag{2.28}$$

Where the electron charge magnitude is $e=1$ in relative units and the background density is $\rho_b(\Omega)=\frac{+N_e}{4\pi R^2}$. Ω_i labels the angular coordinates of electron i. Like in (2.27), this expression can be easily simplified to obtain the correction in units of $\frac{e^2}{l_0}$:

$$E_{eb}+E_{bb}=-N_e^2\sqrt{\frac{\nu}{2N_e}} \tag{2.29}$$

The correction $E_{ee}+E_{eb}$ obtained from (2.28) is added to QP, QH and the ground state energies unlike A_q, which is only subtracted from the QP and QH energies. The various coulomb and short-range considered in this study, along with the corresponding finite-size corrections are listed in the table below.

Interaction	A_q	$E_{eb}+E_{bb}$
Coulomb $V(r)=\frac{1}{r}$	$-\frac{q^2}{2R}$	$\frac{-N_e^2}{2R}$
Yukawa $V(r)=\frac{e^{-\kappa r}}{r}$	$-\frac{q^2}{4\kappa R^2}\left(1-e^{-2\kappa r}\right)$	$-\frac{N_e^2}{4\kappa R^2}\left(1-e^{-2\kappa r}\right)$
Modified Gaussian $V(r)=\frac{1}{r}e^{-r^2/\sigma^2}$	$-\frac{q^2\sigma}{4R^2}\sqrt{\frac{\pi}{2}}erf\left(\frac{\sqrt{2}R}{\sigma}\right)$	$-\frac{N_e^2\sigma}{4R^2}\sqrt{\frac{\pi}{2}}erf\left(\frac{\sqrt{2}R}{\sigma}\right)$
Modified Power-Law $V(r)=\frac{1}{(r^2+a^2)^{\frac{\nu}{2}}}$	$-\frac{q^2}{8R^2}\left(\frac{(4R^2+a^2)^{1-\frac{\nu}{2}}-(a^2)^{1-\frac{\nu}{2}}}{1-\frac{\nu}{2}}\right)$	$-\frac{N_e^2}{8R^2}\left(\frac{(4R^2+a^2)^{1-\frac{\nu}{2}}-(a^2)^{1-\frac{\nu}{2}}}{1-\frac{\nu}{2}}\right)$

Table 2.2: Finite-size corrections to the energy for the interactions considered in this work. The corrections are reported in units of $\frac{e^2}{l_b}$ and are normalized by a factor of $\frac{2Q\nu}{N_e}$ to obtain the final values

2.3 Cylindrical Geometry

For the purposes of infinite-system Density Matrix Renormalization group, we consider the infinite cylinder geometry as discussed in Zaletel et al. [16], which consists of a cylinder with infinite extent along its axis in the y-direction and a finite circumference in the x-direction L_x, which defines the length scale for this system. This geometry allows us to map the 2D FQH

problem onto a 1D chain of Landau orbitals well-suited for DMRG (discussed in section 2.4). Unlike the sphere, the cylinder has zero curvature effects [17], making it more efficient for extrapolating findings to the planar 2D thermodynamic limit. Moreover as the infinite cylinder has no boundaries, every point on the surface experiences uniform bulk properties. The absence of confining potentials and other edge effects helps preserve the translational symmetry of the interaction Hamiltonian (which depends only on the relative separation between particles).

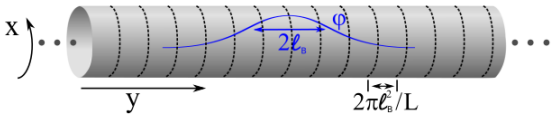

Figure 2.2: Schematic for Landau orbitals along an infinite cylinder. Reproduced from Ref. [16] Copyright © American Physical Society.

Following the construction in [16], the Landau states for electrons on the cylinder surface subject to a uniform radial magnetic field $B(\hat{z})$, we consider the Landau gauge $\vec{A} = (-Bx, 0)$ for which the system maintains translational symmetry along the circumference L_x, leading to conservation of momentum in the x-direction. Thus we consider the plane-wave ansatz $\psi(x,y) = e^{ikx} f(y)$ where $f(y)$ describes the localization of the state along the axis. On substituting this into the Hamiltonian given by (1.1), the kinetic energy term reduces to a harmonic oscillator along y direction centered at $y = kl_b^2$ for magnetic length $l_b = \sqrt{hc/eB}$. Moreover as the system repeats along the x-direction we apply the periodic boundary conditions $\psi(x + L_x, y) = \psi(x,y)$ following which we obtain the allowed values for the quantized x-momentum $k_n = \frac{2\pi n l_b^2}{L_x}$ for integer n. Each Landau orbital can thus be labeled by the integer n that specifies its x-momentum k_n, which in turn determines its position y_n along the cylinder axis. The exact expression for the Landau orbital is

$$\phi_n(x,y) = \frac{1}{\sqrt{L_y \ell_B \sqrt{\pi}}} e^{ik_n x} e^{-\frac{(y-y_n)^2}{2\ell_B^2}} \tag{2.30}$$

Thus, the wavefunction for orbital n has a Gaussian profile centered at guiding-center position y_n with the spacing between the orbitals determined as $\Delta k = k_{n+1} - k_n = \frac{2\pi l_b^2}{L_x}$. Thus, each orbital becomes a site in a 1D lattice with occupation $n_i = 0, 1$ which allows us to implement iDMRG using the Matrix-Product State (MPS) formalism.

The interaction Hamiltonian in second quantization is expressed as the sum over two-body matrix elements $V_{n_1 n_2 n_3 n_4}$ analogous to (2.21), where the orbitals participating in the scattering are labeled by momentum indices n_i that represent their guiding-center coordinates along the axis. Since each orbital is a plane-wave in the periodic x-direction $e^{ik_n x}$, the matrix elements are non-zero only when $n_1 + n_2 = n_3 + n_4$, thus enforcing the conservation of the total momentum in x-direction.

Furthermore, the interaction is also translationally symmetric in the y-direction, which requires the Hamiltonian to remain invariant under the transformation $T : n_i \to n_i + 1$ that shifts each orbital index by one unit. This implies that the matrix elements depend only on orbital separations instead of their absolute positions, which allows us to express the Hamiltonian using the relative indices $k = n_2 - n$ and $m = n_1 - n$ for the choice of the reference orbital labeled by $n = n_4$. The expression for the Hamiltonian as given by [16] is

$$H = \sum_{n} \sum_{k,m} V_{k,m}\, c^{\dagger}_{n+m} c^{\dagger}_{n+k} c_{n+m+k}\, c_n \tag{2.31}$$

where n labels the position of the interacting pair of particles along the cylinder.

From [16], the matrix elements $V_{k,m}$ obtained by integrating over the coordinates of the two particles are of the form $V_{k,m} \propto f(k,m) e^{-2\pi^2(k^2+m^2)/L^2}$, where the exponent arises from the overlap between the Gaussian Landau orbitals with relative separations that depend on k and m. Thus, the matrix elements are exponentially suppressed for orbitals far apart, making the interaction effectively short-ranged along the orbital chain. For small values of circumference L_x, orbitals are far apart and the interactions are short-ranged, whereas a larger circumference corresponds to a longer interaction range by decreasing the orbital spacing.

In the case of a thin cylinder with $\mathrm{L} \to 0$ (referred to as the Tao-Thouless limit), the overlap between the Gaussian orbitals becomes negligibly small. As a result, the off-diagonal elements in (2.31) are suppressed and the dominant terms in the Hamiltonian are the density-density interactions, expressed as

$$H \approx \sum_{i<j} U_{i-j} n_i n_j \tag{2.32}$$

where the number operator $n_i = c_i^{\dagger} c_i$ represents the electron density at site i. Since the interaction Hamiltonian becomes diagonal in occupation-number basis, it reduces to a classical electrostatic interaction between electrons with fixed positions along a 1D lattice, as noted in Misguich et al. [18]. Instead of a superposition of many-body occupation states, the ground state is provided by a single configuration of electrons that minimizes electrostatic repulsion. This configuration is referred to as the 'root configuration'. The ground states for different filling fractions reduce to different root configurations in the thin-cylinder limit. For instance, the ground state configuration for the Laughlin state $\nu = 1/3$ in this limit arises from evenly distributing one electron every three orbitals to minimize energy, resulting in a root configuration of the form 010 010 010 010 etc.

2.4 Infinite-system DMRG (iDMRG)

For the purposes of this study, we used the infinite-system DMRG code developed by Roger S.K. Mong and Michael P. Zaletel for ground-state energy calculations within the TeNPy tensor-network framework [19]. The excited-state calculations were performed using a segment

DMRG code that we modified to construct quasi-hole/quasi-particle excitations, as described in section 2.5. The infinite-system DMRG is an iterative algorithm that converges to the ground state, which, in the tensor-network formalism, can be understood as a variational optimization over a class of objects called Matrix-Product States (MPS) [20]. I begin by providing a brief overview of the salient features of MPS, following the review by Schöllwock [20].

The general representation of the many-body wavefunction in the chosen basis consisting of N Landau orbitals along the cylinder is

$$|\psi\rangle = \sum_{n_1,n_2,\ldots,n_N} C_{n_1 n_2 \ldots n_N} |n_1 n_2 \ldots n_N\rangle \tag{2.33}$$

where $|n_i\rangle$ represents the local basis at site i with $n_i = 0$ and 1 corresponding to empty and occupied orbitals. The coefficient $C_{n_1 n_2 \ldots n_N}$ form a rank-N tensor with 2^N entries, thus growing the Hilbert space exponentially with system size. Since operating on the full coefficient tensor is inefficient for large systems, the MPS formalism is used to factorize the coefficient tensor into a product of smaller tensors, significantly reducing computational cost by providing an alternate way to represent the wavefunction with fewer parameters.

The MPS decomposition is obtained by repeatedly applying singular value decomposition (SVD) to the coefficient matrix after grouping indices as

$$C_{n_1,(n_2 \ldots n_N)} = \sum_{\alpha_1} U_{n_1,\alpha_1} \lambda_{\alpha_1} V_{\alpha_1,(n_2 \ldots n_N)} \tag{2.34}$$

where the degrees of freedom for the first site are separated from the remaining system. By defining the tensor $A^{n_1}_{\alpha_1} = U_{n_1,\alpha_1}$ and repeating the process for the remaining indices, we obtain the matrix product representation

$$|\psi\rangle = \sum_{n_1,\ldots,n_N} \sum_{\alpha_1,\ldots,\alpha_{N-1}} A^{n_1}_{\alpha_1} A^{n_2}_{\alpha_1 \alpha_2} \cdots A^{n_N}_{\alpha_{N-1}} |n_1 n_2 \ldots n_N\rangle. \tag{2.35}$$

Where the coefficient matrix is written as a product of rank-3 MPS tensors, with each tensor possessing a physical index representing the site occupation, along with auxiliary bond indices α_i connecting neighboring tensors. Following [20], performing SVD at each step is equivalent to the Schmidt decomposition across the bond connecting neighboring sites. This defines the division of the Hilbert space into left and right sectors across the bond, represented by the orthonormal bases $|\alpha_L\rangle$ and $|\alpha_R\rangle$. The state can thus be written as

$$|\psi\rangle = \sum_{\alpha=1}^{\chi} \lambda_\alpha |\alpha_L\rangle |\alpha_R\rangle \tag{2.36}$$

where the bond dimension χ quantifies the number of Schmidt coefficients λ_α that we retain every time the system is partitioned across a bond. Since the Schmidt rank determines entanglement between the two subsystems, truncating the bond dimension limits the entanglement

that can be represented across a bond. The resulting approximation error is provided by the weight of the discarded Schmidt coefficients $1-\sum_i \lambda_\alpha^2$.

Extending this formulation [20], many-body operators can also be written in a tensor-network representation as a product of local tensors known as Matrix Product Operator (MPO). Analogous to (2.35) operators can be expanded in the ket-bra basis states as

$$\hat{O} = \sum_{\{n_i,m_i\}} O^{m_1\ldots m_N}_{n_1\ldots n_N} |n_1 n_2 \ldots n_N\rangle\langle m_1 m_2 \ldots m_N| \tag{2.37}$$

Where the operator coefficients are factorized into local tensors $W^{[i]}$ as

$$O^{m_1\ldots m_N}_{n_1\ldots n_N} = \sum_{\{\alpha_i\}} W^{[1]\,n_1 m_1}_{\alpha_1} W^{[2]\,n_2 m_2}_{\alpha_1\alpha_2} \cdots W^{[N]\,n_N m_N}_{\alpha_{N-1}} \tag{2.38}$$

The physical ket and bra indices n_i and m_i in (2.38) describe the local operator action. The dimension of the auxiliary bond index α_i, defines the MPO bond dimension D, which determines the complexity of the operator representation by specifying the number of possible operator 'channels' propagating across the bond. In particular, Hamiltonians for finite-ranged interactions are represented as MPO's with small bond dimensions. The MPO decomposition provides an efficient way to store and manipulate many-body operators. In algorithms like DMRG, quantities like expectation values can be directly computed by contracting MPS and MPO tensors along the chain.

A brief outline of the infinite-system DMRG algorithm is provided here, adapted from the discussion in Hauschild and Pollmann [19]. Instead of operating on a large system with many sites (as in finite DMRG), iDMRG represents the system as an infinite repetition of a finite unit-cell. Each unit cell is a block of L orbitals that makes up the infinite system when repeated periodically, represented in tensor-network formalism as a periodic chain of repeating MPS/MPO tensors. This periodicity follows from the assumption that the ground-state wavefunction of the infinite orbital chain is invariant under translation by L orbitals.

For a general many-body state, the entanglement entropy across a bond partitioning the system into two subsystems A and B is $S_A = -Tr(\rho_A log \rho_A)$ (where ρ_A is the reduced density matrix for subsystem A), which can be expressed in terms of the Schmidt coefficients as $S = -\sum_\alpha \lambda_\alpha^2 \log \lambda_\alpha^2$ [19]. As detailed in Eisert et al. [21], for gapped systems like the FQH phase, the entanglement entropy obeys the 'area law' $S_A \sim |\partial A|$ where $|\partial A|$ is the size of the boundary separating the subsystems. Since the boundary between subsystems for the cylinder is simply a circle around the cylinder, the entanglement entropy scales with cylinder circumference $S \sim L_y$, resulting in a finite entanglement across an MPS bond even for an infinite-length system. This allows us to efficiently represent the ground-state with an MPS with finite bond dimension.

Starting with an initial MPS ansatz for the wavefunction, the algorithm proceeds to iteratively optimize a few tensors at a time by variationally minimizing the energy $E = \langle\psi|H|\psi\rangle$

within a MPS manifold of fixed bond dimension. This is implemented by performing an 'n-site update' ($n = 2$ in our considerations) consisting of solving a local eigenvalue problem for the effective Hamiltonian, followed by singular value decomposition (SVD) to project back to the variational space of the MPS by truncating the bond dimension [16].

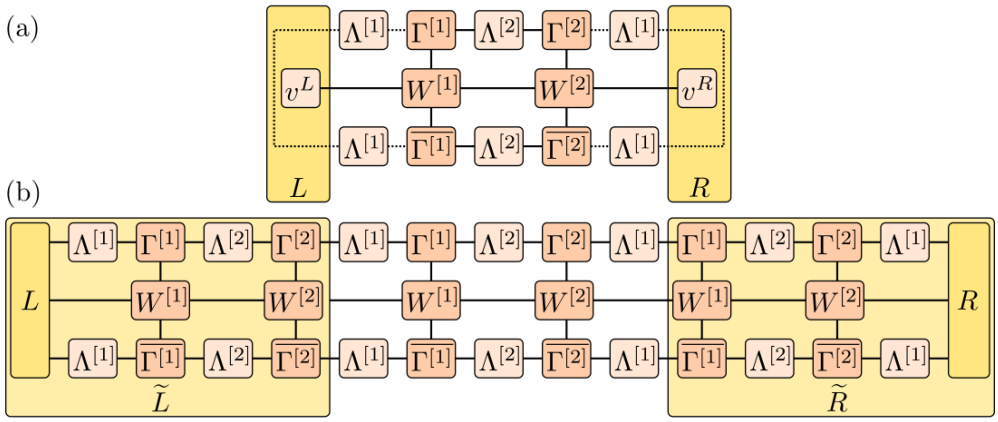

Figure 2.3: Tensor network structure for iDMRG with unit cell length $L = 2$. Reproduced from Hauschild and Pollmann [19] Copyright © American Physical Society. The wavefunction is represented as an infinite MPS composed of MPS tensors $\Gamma^{[i]}$ and diagonal matrices $\Lambda^{[i]}$ containing the Schmidt coefficients residing on the MPS bonds. The shaded portions represent the left and right environments, which effectively approximate the contributions from the semi-infinite portions of the chain on either side of the 2-site optimization window. The $W^{[i]}$ matrices are the local MPO tensors representing the Hamiltonian, which are terminated on both ends by the boundary vectors v^L and v^R.

Following the treatment in [19], the iDMRG algorithm proceeds through the optimization of tensors within a finite window of sites (represented by the unshaded portion in Fig.2.3(a)). The remainder of the chain is encoded in the left and right environments, which provide the boundary conditions during the optimization step. The iDMRG algorithm implemented in this study can be summarized in the following steps:

1. Two-site optimization: The algorithm starts with optimizing two neighboring tensors within the unit cell (which forms the finite window for optimization) while keeping the left and right environments fixed. Mathematically, the two-site wavefunction can be represented as the coefficient matrix $\Theta^{n_i n_{i+1}}_{\alpha\beta}$ which can be constructed from the neighboring MPS tensors as

$$\Theta^{n_i n_{i+1}}_{\alpha\beta} = \sum_{\gamma} \Gamma^{[i]n_i}_{\alpha\gamma} \Lambda^{[i]}_{\gamma} \Gamma^{[i+1]n_{i+1}}_{\gamma\beta} \tag{2.39}$$

where n_i and n_{i+1} are the physical indices for the two sites. This tensor is optimized to find the lowest-energy tensor compatible with the current environments. This is accomplished by solving the local eigenvalue problem $H_{\text{eff}}|\Theta\rangle = E|\Theta\rangle$, where the effective

Hamiltonian is constructed using the local MPO tensors and the current environments as

$$H_{\text{eff}} = L \cdot W^{[i]} \cdot W^{[i+1]} \cdot R \tag{2.40}$$

where the environments L and R are the contractions of the MPS and MPO tensor chains outside the optimization window. Fig. 2.3(a) represents the action of the effective Hamiltonian on the state, represented as contraction of the operators $W^{[i]}$ with the unit-cell tensors $\Gamma^{[i]}$. Following this, the optimized tensor is restored back to the MPS form by reshaping the indices and performing SVD analogous to equation (2.33) to obtain $\Theta = USV^{\dagger}$ where the retained Schmidt coefficients (determined by bond dimension χ) forms the new Schmidt matrix $S = \Lambda^{[i]}$ and the updated site tensors become $\Gamma^{[i]}$ and $\Gamma^{[i+1]}$.

2. DMRG sweeps and environment updates: The two-site optimization described in step 1 is applied successively across all the bonds in the unit cell, which for unit-cell length L corresponds to updates involving the site pairs labeled by physical indices (1, 2), (2, 3), (3, 4)... $(L-1, L)$. This constitutes a single DMRG sweep over the unit cell. Once the sweep is completed, the optimized unit cell is absorbed into the left and right environments as seen in Fig. 2.3(b), by contracting the unit cell tensors with the existing environments. Thus, the environments get updated to include the latest tensor information as $L \to \tilde{L}$ and $R \to \tilde{R}$.

3. System growth and convergence: In the beginning, the environment tensors only contain contributions from a small number of unit cells, thus only providing an approximate description of the semi-infinite systems on the left and right. Each time an optimized unit cell is absorbed following steps 1 and 2, the updated environments contain information corresponding to increasingly larger sections of the chain. Once the tensors stop changing upon absorbing additional unit cells ($\tilde{L} \approx L$ and $\tilde{R} \approx R$), the system is set to attain convergence. The resulting MPS corresponds to the true ground state of the infinite system with translational symmetry over L sites. The environments at this stage become fixed-point tensors representing the infinite repetition of unit cell tensor in the left/right directions.

The MPS in our iDMRG construction was initialized using the product state ($\chi = 1$) corresponding to the root configuration for various filling fractions as discussed in section 2.3. This allows the algorithm to start with low-entanglement states and to build entanglement gradually through optimization, leading to more stable convergence. The root configuration also determines the unit cell length for a particular filling fraction, since it corresponds to a single, unique particle distribution that is repeated periodically.

Long-range interactions are difficult to represent as MPO tensors as contractions become computationally expensive for large MPO bond dimensions. To make the long-ranged coulomb interaction effectively finite-ranged, it was multiplied by the Gaussian cutoff $V(r) \to \frac{1}{r} e^{-r^2/2\xi^2}$.

Furthermore, the interactions were decomposed using the exponential approximation $V(r) \approx \sum_k a_k e^{-b_k r}$ since exponentials are easier to store in the MPO representation due to small bond dimension. The accuracy of this approximation was set by the tolerance parameter ε defined as $|V_{exact}(r) - V_{approx}(r)| < \varepsilon$, which in our case was set to 10^{-5}.

2.5 Quasi-Holes and Quasi-Particles in segment DMRG

To construct the excited states, we implement segment DMRG, wherein a segment of length L is extracted from the converged ground-state MPS obtained from the iDMRG algorithm. The segment is embedded between environments representing the semi-infinite ground state on the left and right sides. The segment is then modified by altering the MPS tensors to construct the quasi-hole and quasi-particle excitations. This is followed by DMRG optimization of the finite central region containing the segment tensors while the environments are kept fixed, producing a localized excitation in an infinite ground state.

As detailed in [16], the MPS construction conserves two quantum numbers across the orbital chain, the particle number C (also referred to as charge) and the guiding center momentum K. These symmetries are enforced by assigning these quantum numbers to the MPS tensor indices, which are partitioned into sectors labeled by the conserved quantum numbers $q = (C,K)$. Here we consider the sectors assigned to the physical index as q_P, which consists of a fixed set of (C,K) values corresponding to filled and empty orbital occupations $n_i = 0$ or 1. On the other hand, the auxiliary bond sectors (represented as q_L and q_R depending on whether they reside on the left or right bond of the MPS tensor) represent the cumulative charge and momentum to the left of the bond. Non-zero tensor elements are only allowed when the sectors residing on the corresponding tensor's bond indices follow the charge conservation rule $q_L + q_P - q_R = q_{total}$ where q_{total} is the total charge of the tensor, making the tensors block-sparse.

For ground-state MPS, the tensors are neutral with respect to the quantum numbers, thus satisfying the conservation rule $q_L + q_P = q_R$. For quasi-hole and quasi-particle states, the tensor at the excited site carries a net, non-zero set of quantum numbers $q_{total} = (\Delta K, \Delta C)$ that reflects the change in total charge/momentum across the segment on introducing the QH/QP excitation.

Assuming all MPS tensors to be neutral, the charge conservation $q_L + q_P = q_R$ can be applied across all the tensors to obtain the total segment charge and momentum in terms of the quantum numbers assigned to the physical indices q_p. Following [16], the quantum numbers for q_P can be written as $(K,C) = (jq(j), q(j))$ where $q(j)$ is the physical charge that depends on the occupation of the orbital at site j, and the momentum is simply the product of the charge and the site index j. The total charge and momentum across the segment can then be expressed as

$$\Delta C_{segment} = \sum_j q(j) \tag{2.41}$$

$$\Delta K_{segment} = \sum_j j \cdot q(j) \tag{2.42}$$

where j sums over the segment tensor indices 0 to $L-1$. In the MPS, $\Delta C_{segment}$ and $\Delta K_{segment}$ simply corresponds to the difference in charge and momentum quantum numbers of the right and left boundary bonds of the segment that connect to the environment. To maintain charge neutrality for the ground-state, the physical charge associated with site j for filling fraction $1/3$ is normalized as $q(j) = 3n(j) - 1$ where $n(j) = 0, 1$ is the site occupation. The on-site physical charge for different filling fractions is normalized differently so that the net charge across a unit cell sums to zero. For instance, the ground state segment for the filling fraction 2/5 has physical charges 2 and -3 associated with empty and filled occupations. The unit cell for this case is represented in the thin-torus limit as the root configuration 01010, which by taking into account the charges assigned to the unit cell orbitals turns out to be charge-neutral. The same principle applies to the momentum quantum number.

Fig.2.4 illustrates the flow of charges and momenta for a ground-state segment ($L = 6$) constructed from the root configuration for $\nu = 1/3$. The physical charges and momenta across all the sites sum to zero, resulting in the same charge sector $(0,0)$ on the left and right boundary bonds connecting to the environments L and R.

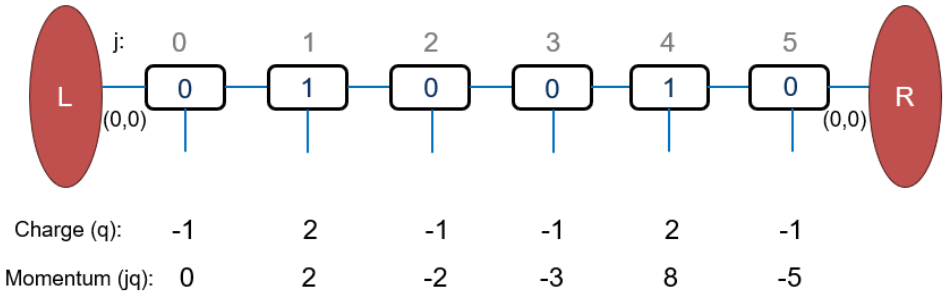

Figure 2.4: Charge and momentum quantum numbers for GS segment constructed from root configuration

To construct the quasi-hole, an extra tensor corresponding to occupation 0 in the root configuration is added in the middle of the segment as shown in Fig.2.5. As a result, the MPS tensors to the right of the added site, along with the right environment get shifted by one unit to the right. The boundary bond connected to the right environment gains extra charge and momentum represented as $(-3,-1)$ whereas the right environment expects $(0,0)$. This sector mismatch is removed by absorbing the excess charge at the QH tensor site. The QH tensor is then constructed by selecting blocks corresponding to sector combinations that give a total contribution $q_{total} = (-3,-1)$.

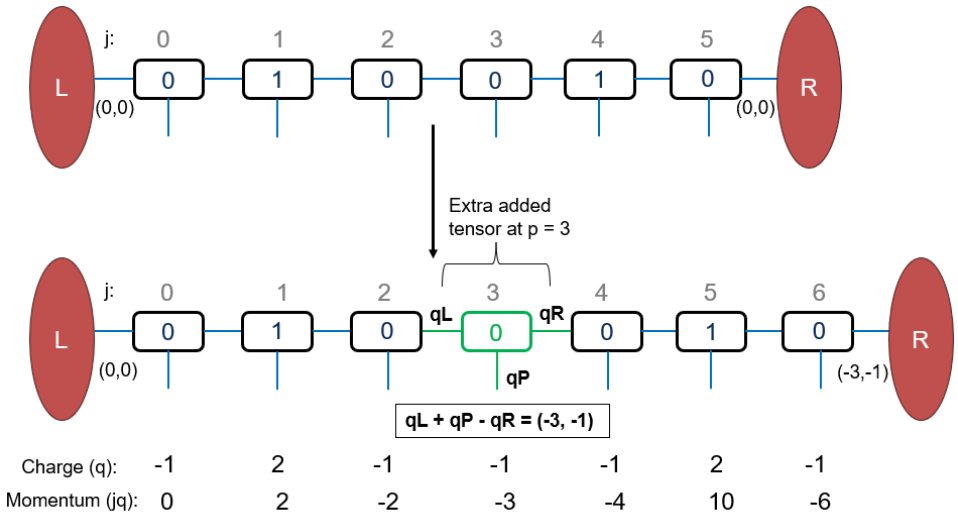

Figure 2.5: Charge and momentum quantum numbers for QH segment constructed from root configuration

A similar construction is applied for the case of the quasi-particle, which in the root configuration is constructed by removing an orbital with occupation 0. This corresponds to shifting all MPS tensors right of the removed site by one unit to the left. The resulting mismatch in charge and momentum quantum numbers across the segment is used to construct the QP tensor as shown in Fig.2.6

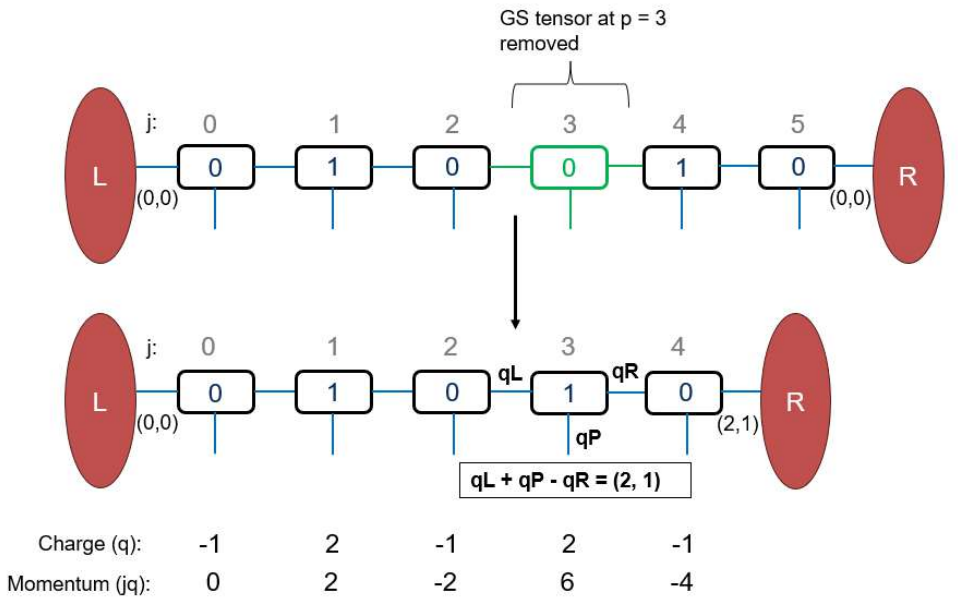

Figure 2.6: Charge and momentum quantum numbers for QP segment constructed from root configuration

The QH and QP construction outlined above is generalized to a segment of length L. The tensor at the excitation site is constructed explicitly by calculating the total charge and mo-

mentum across the segment for the root configuration with L sites, and compatible blocks are initialized with random entries. A suitable segment length was chosen so as to capture the complete charge profile of the quasi-hole/quasi-particle excitation along with the corresponding charge deficit/excess. This was obtained by computing the difference between the net charge contained by the converged QH/QP segment and the corresponding GS segment MPS at fixed L, followed by running DMRG for different segment lengths L till the required charge difference was obtained (-1/3 and +1/3 for QH and QP excitations at $\nu = 1/3$).

This process was repeated after systematically increasing the cylinder circumference L_x, so as to obtain finite-system data at different system sizes for thermodynamic extrapolation. At each L_x, the GS segment energy along with the energy of the modified segment consisting of the added/removed site was obtained using DMRG. The gap was calculated using the expression analogous to the one used in spherical ED [15]:

$$\Delta_{\text{charge}} = \frac{E(L-1) + E(L+1) - 2E(L)}{n_q} \tag{2.43}$$

where n_q is the number of quasi-holes/quasi-particles corresponding to adding/removing a single orbital from the segment with L sites. For Jain states $\nu = p/2p+1$, $n_q = p$.

For each considered L_x, several DMRG runs were conducted for increasing values of bond dimension χ, and the process was terminated to obtain the converged gap when the difference between the gap values obtained from successive iterations was less than 10^{-4}. Since the entanglement on the cylinder grows with L_x, the bond dimension of the corresponding segment MPS tensors also increases. The maximum bond dimension considered for this study was 2048, corresponding to system size $L_x = 24\ l_b$ at 1/3 filling.

Chapter 3

Results and Discussion

3.1 Exact Diagonalization on Sphere

As a benchmark, the energies and excitation gaps for the V1 Haldane pseudopotential interaction were calculated to verify whether the obtained gap values were consistent with the form of the Laughlin ansatz.

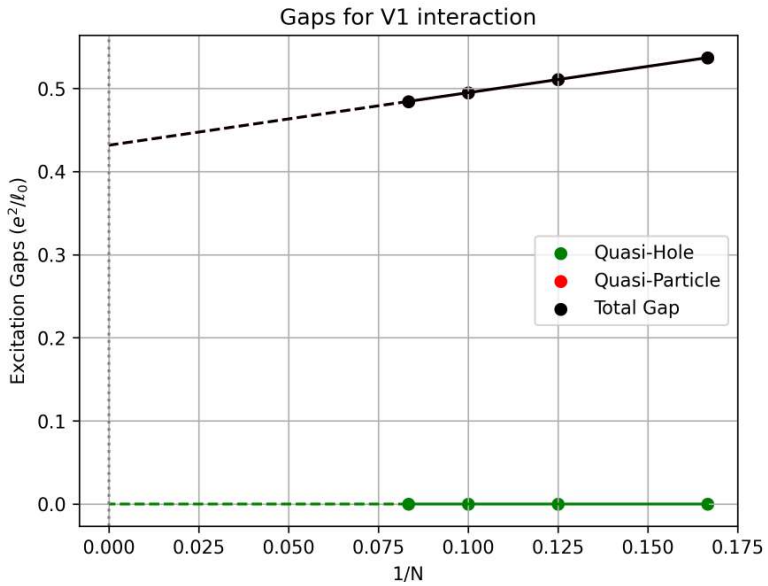

Figure 3.1: Excitation gaps vs. $\frac{1}{N_e}$ for V1 interaction, $\nu = \frac{1}{3}$

The ground state energies obtained were zero as expected since the Laughlin state is the exact ground state for this interaction. Moreover, the energy required to create the quasi-hole excitation is also zero as shown in fig. 3.1, where the only contribution to the charged excitation gap is the quasi-particle energy. This is consistent with the Laughlin wavefunction, since the V1 pseudopotential only penalizes pairs of particles having relative angular momentum $m = 1$ and the Laughlin ansatz (1.4) eliminates all such pairs. Since the quasi-particle involves multiplying the wavefunction by a factor of $\prod_i (z_i - \eta)$, no $m = 1$ pairs are introduced, and the ground state

and QH energies are both zero. QP wavefunctions on the other hand include such pairs due to the presence of the derivatives with respect to particle coordinates $\prod_i \frac{\partial}{\partial z_i}$ that lowers the polynomial degree.

To verify whether the ground state correction and energy normalization was applied correctly, the per-particle coulomb energies were plotted against $\frac{1}{N_e}$ to obtain the thermodynamic estimates.

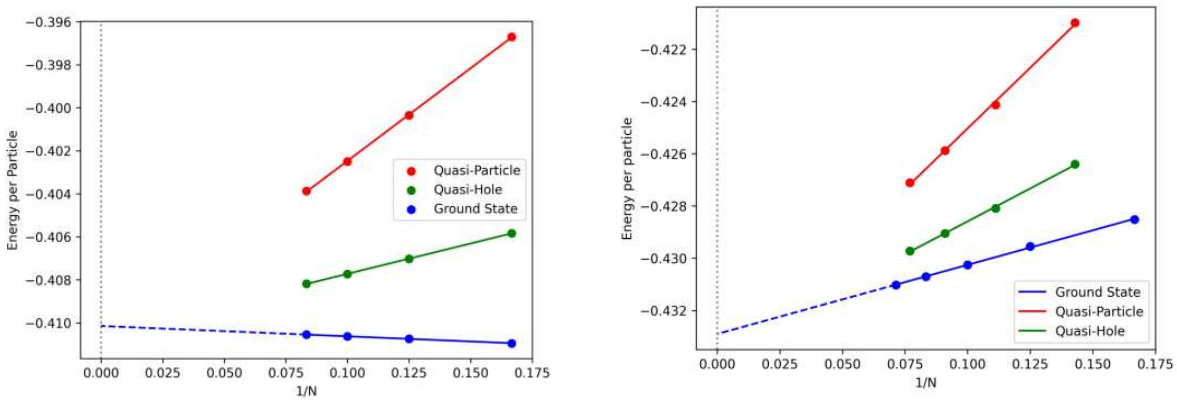

(a) (b)

Figure 3.2: Per-particle ground state and excited state energies vs. $\frac{1}{N_e}$ for $\nu = \frac{1}{3}$ (a) and $\frac{2}{5}$ (b). The obtained coulomb GS energy estimates for the same are -0.41015 e^2/l_0 and -0.432901 e^2/l_0 respectively, that match the values from Haldane and Rezayi [3], Jain and Kamilla [22]

.

The excitation gaps for the coulomb interaction case were obtained as outlined in section 2.2, and the thermodynamic estimates obtained after extrapolating linearly with $\frac{1}{N_e}$ (Fig. 3.3) were found to be consistent with the values previously reported in literature. The gaps for quasi-hole (Δ_{qh}), quasi-particle (Δ_{qp}) and the total excitation gap $\Delta = \Delta_{qp} + \Delta_{qh}$ along with their relative errors from the corresponding values in Morf et al. [4] are tabulated as follows. All energies are expressed in units of e^2/l_0.

ν	Δ_{qp}	Δ_{qh}	$\Delta = \Delta_{qp} + \Delta_{qh}$	**Error**
1/3	0.07489	0.02625	0.10115	0.05%
2/5	0.03984	0.01052	0.05036	0.72%
3/7	0.02689	0.00835	0.03525	0.71%
4/9	0.02102	0.00632	0.02735	1.29%

Table 3.1: Excitation gaps for coulomb interaction obtained from ED

The extrapolated thermodynamic gaps for the Jain states $\left(\nu = \frac{p}{2p+1}\right)$ were plotted against p and $1/(2p+1)$ to obtain the gap scaling on approaching half-filling. As observed in Fig. 3.4, the gaps exhibited significant deviations from the linear 1/(2p+1) scaling that would be expected under constant effective mass.

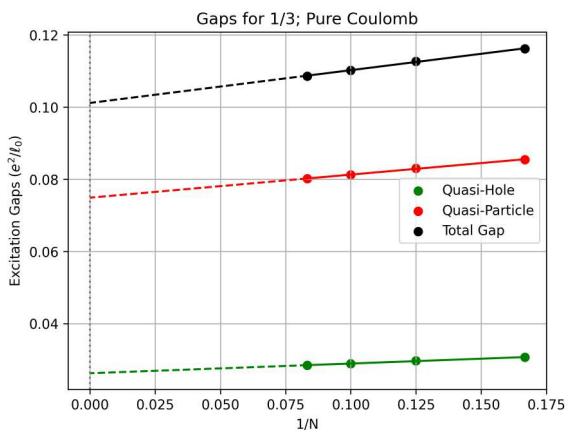

(a)

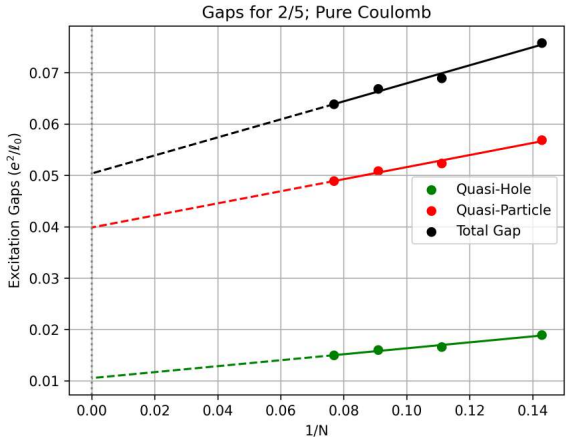

(b)

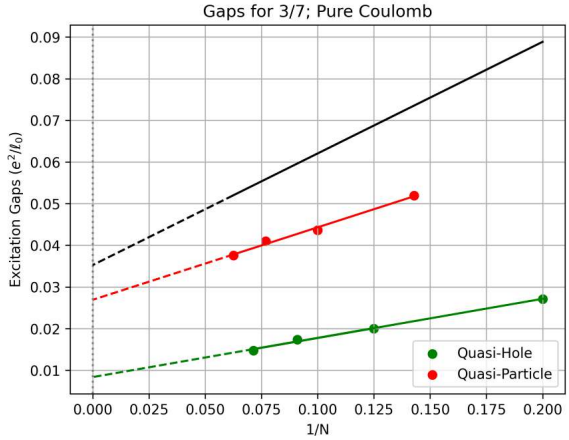

(c)

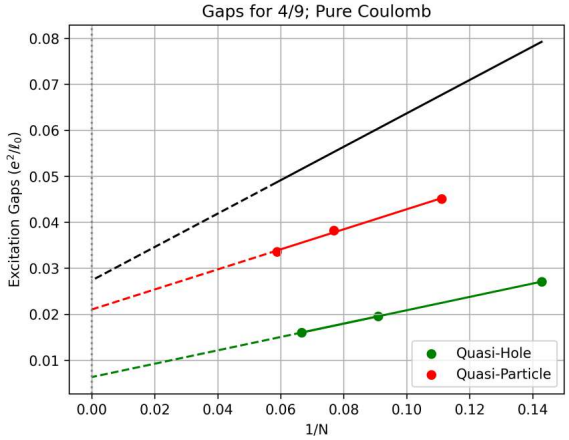

(d)

Figure 3.3: Coulomb interaction gaps linearly extrapolated to thermodynamic limit for different filling fractions

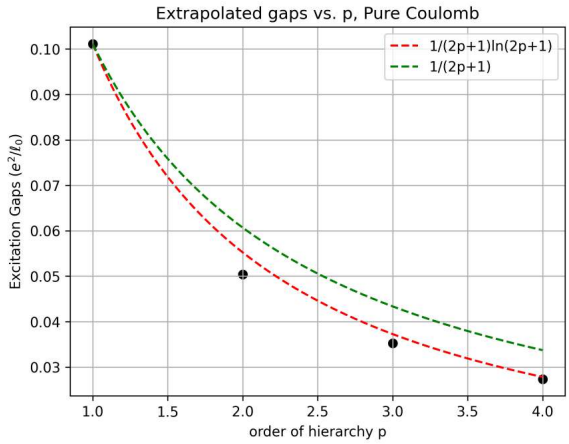

(a)

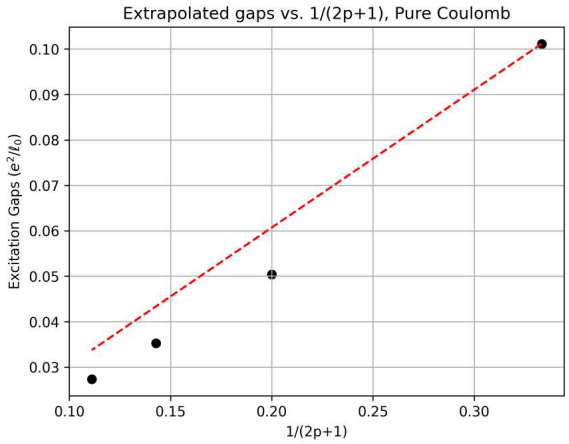

(b)

Figure 3.4: Total thermodynamic charged excitation gaps vs. order p and 1/(2p+1) for coulomb interaction

The effective mass obtained from the gap scaling obtains a logarithmic p-dependence $m^*(p) \propto (2p+1)ln(2p+1)+C$ with $C = 4.078$ obtained by fitting the gap at $\nu = 1/3$. This is consistent with the analysis of the half-filled case by Halperin, Lee and Read [7], where the logarithmic correction in effective mass comes from considering the role of long-wavelength gauge-field fluctuations in mediating interactions between composite fermions.

Extending this procedure, the excitation gaps were computed for short-range interactions involving suppression of the $1/r$ coulomb tail, which as derived in the HLR theory [7] is the source of the logarithmic gap scaling for the coulomb case. Thus, the thermodynamic gap estimates, if obtained could quantify the sensitivity of the coulomb scaling to perturbations in the long-wavelength behavior of the interactions. The interactions considered are as listed in Table 2.2.

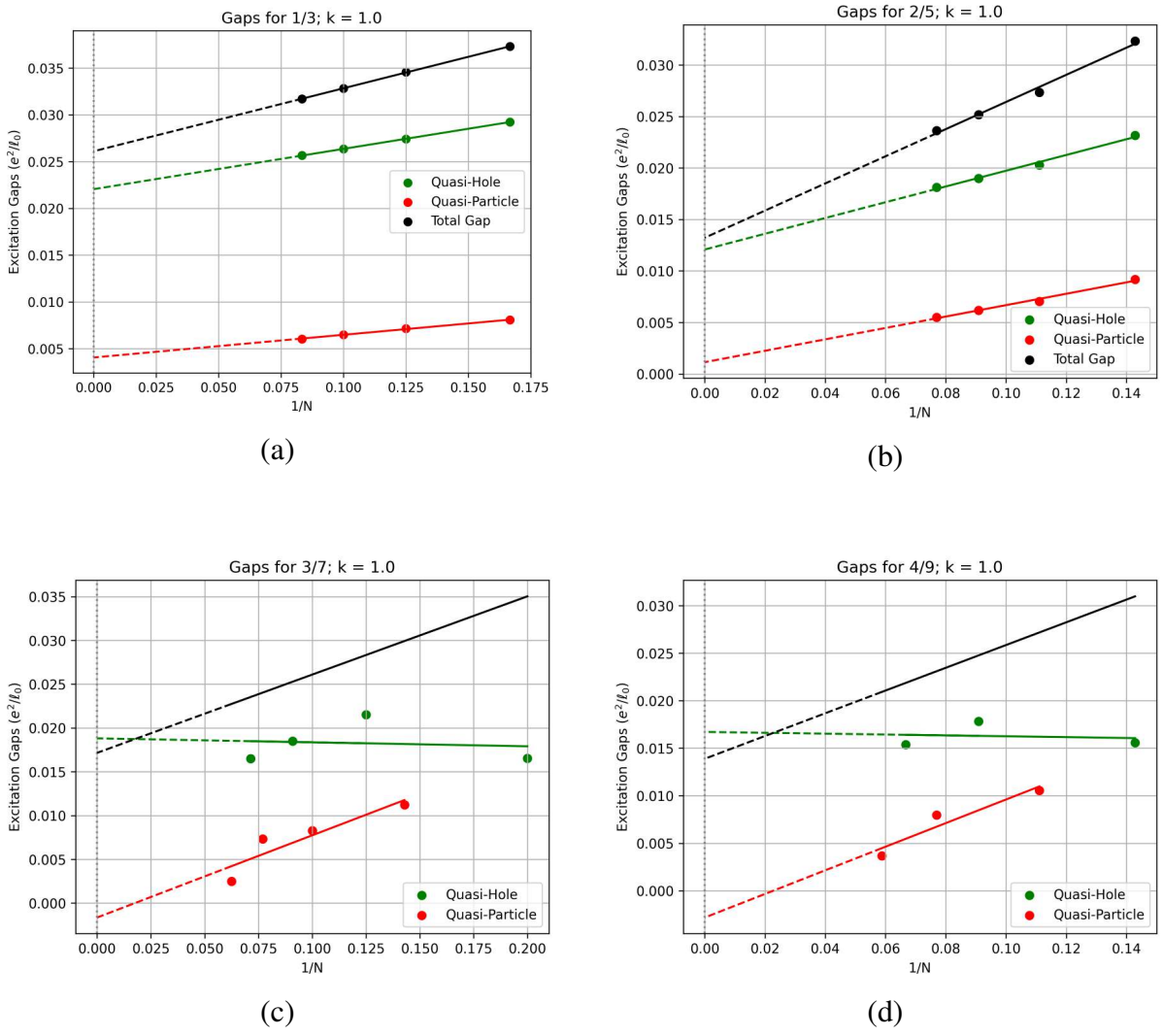

Figure 3.5: Gaps for Yukawa interaction $V(r) = \frac{e^{-\kappa r}}{r}$ for $\kappa = 1.0$, extrapolated linearly to thermodynamic limit for different filling fractions.

For the Yukawa interaction, the obtained QH and QP gaps exhibited strong curvature even for small changes in the screening coefficient κ. The finite-N gaps were well-behaved for linear

extrapolation only for small deviations from the coulomb case such as $\kappa = 0.1$. For larger κ values the thermodynamic estimates from the linear fits became unreliable for $\nu = 3/7$ and $4/9$ as shown in Fig.3.5 (c) and (d). The thermodynamic gaps for the same obtained from quadratic fits for the finite-N data gave small or negative gap values, indicating over-correction for the curvature due to less available system sizes, especially for $\nu = 4/9$ where only three particle numbers could be considered. On the other hand, linear scaling persisted for $\nu = 1/3$ and $2/5$ giving thermodynamic gap values that scaled similarly for both filling fractions on increasing κ.

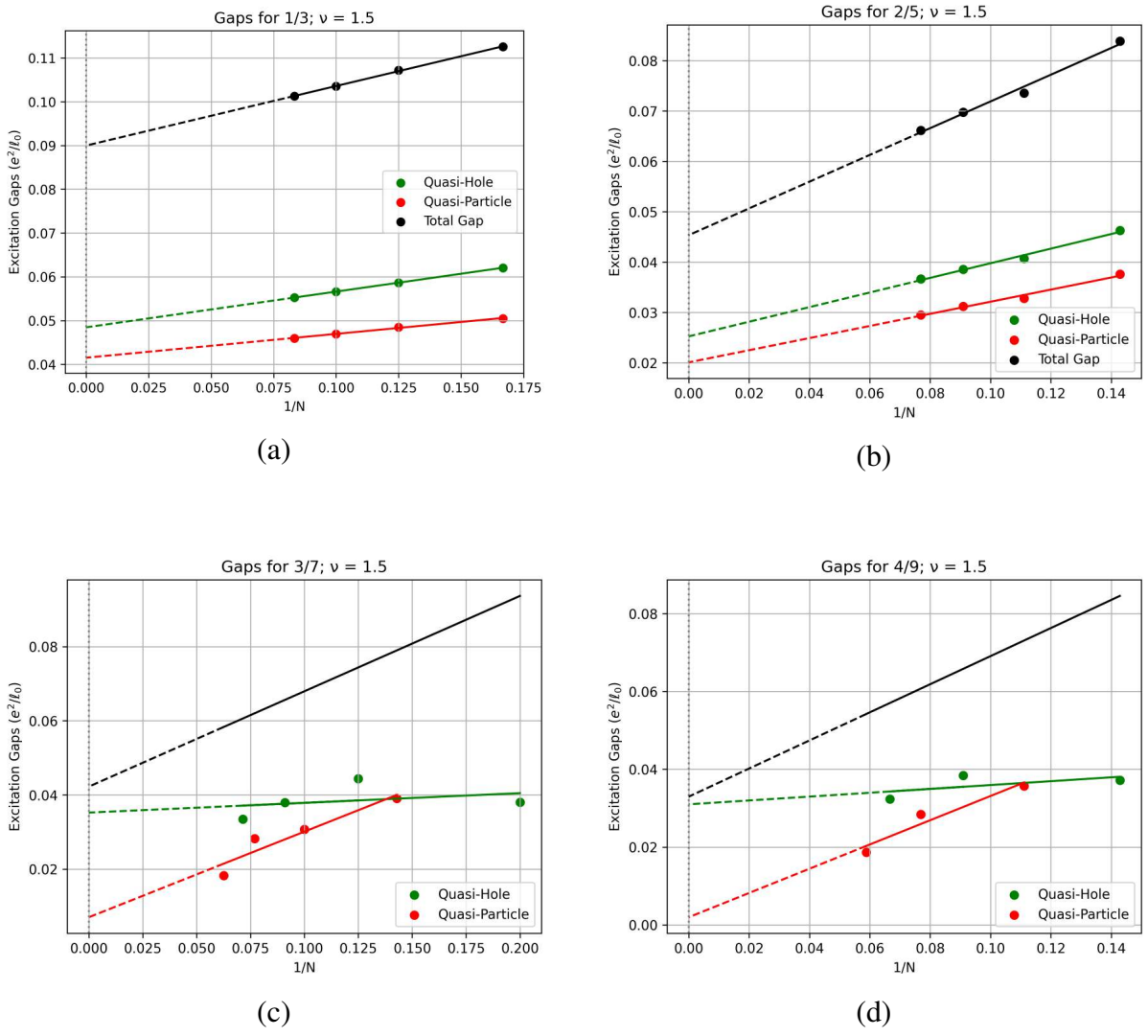

Figure 3.6: Gaps for Power-Law interaction $V(r) = \frac{1}{(r^2+a^2)^{\alpha/2}}$ for $\alpha = 1.5$, extrapolated linearly to thermodynamic limit for different filling fractions.

The form of the power-law interaction $V(r) = \frac{1}{r^n}$ was modified by introducing a small parameter $a = 0.05$ to prevent the spherical pseudopotentials from diverging. As shown in Fig.3.6, thermodynamic estimation failed for $\nu = 3/7$ and $4/9$ as the finite-N data suffered the same problems with finite-sized curvature effects as the Yukawa interaction case.

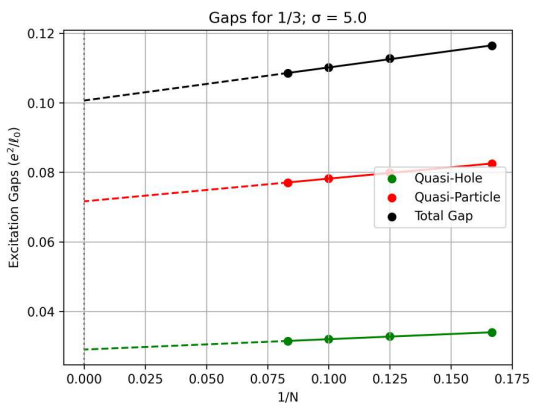

(a)

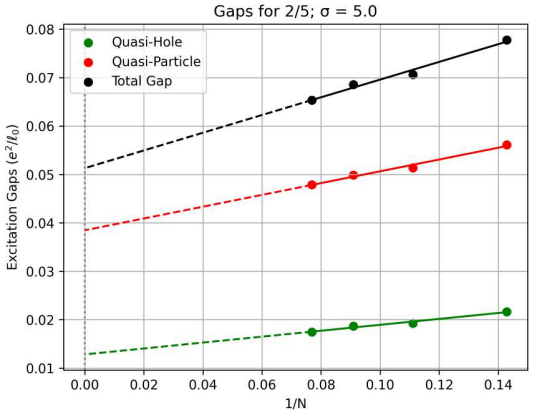

(b)

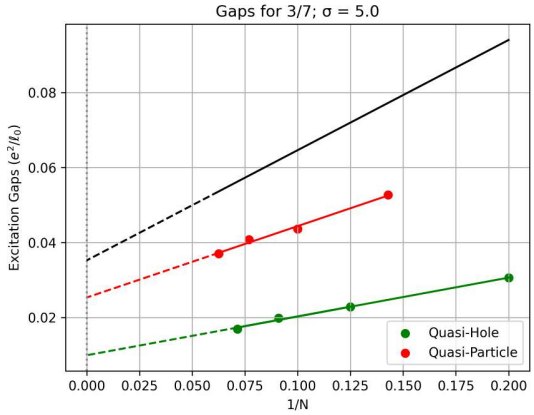

(c)

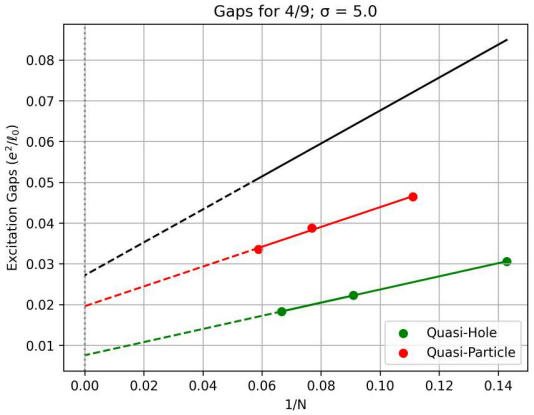

(d)

Figure 3.7: Gaps for modified Gaussian interaction $V(r) = \frac{1}{r} \cdot e^{\frac{-r^2}{2\sigma^2}}$ for $\sigma = 5.0$, extrapolated linearly to thermodynamic limit for different filling fractions.

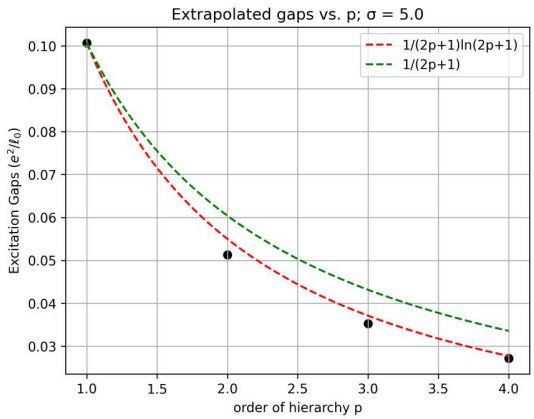

(a)

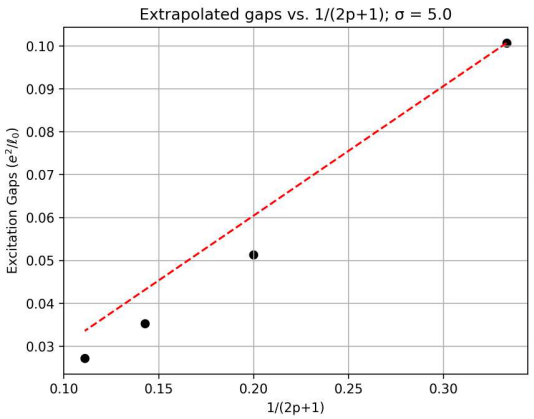

(b)

Figure 3.8: Total thermodynamic charged excitation gaps vs. order p and 1/(2p+1) for modified Gaussian interaction for $\sigma = 5.0$

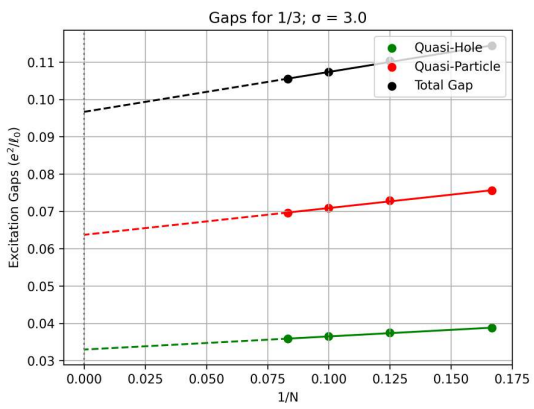

(a)

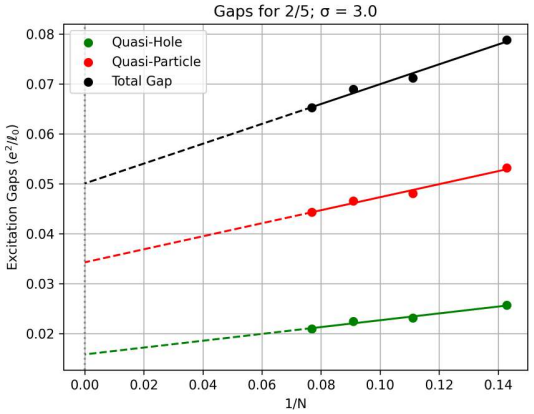

(b)

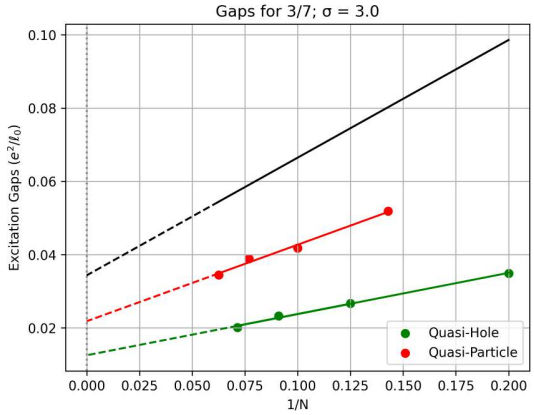

(c)

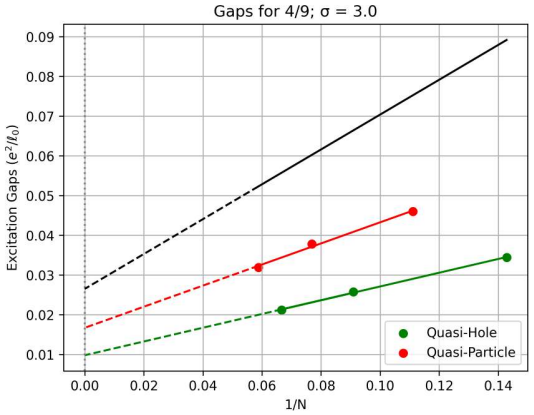

(d)

Figure 3.9: Gaps for modified Gaussian interaction $V(r) = \frac{1}{r} \cdot e^{\frac{-r^2}{2\sigma^2}}$ for $\sigma = 3.0$, extrapolated linearly to thermodynamic limit for different filling fractions.

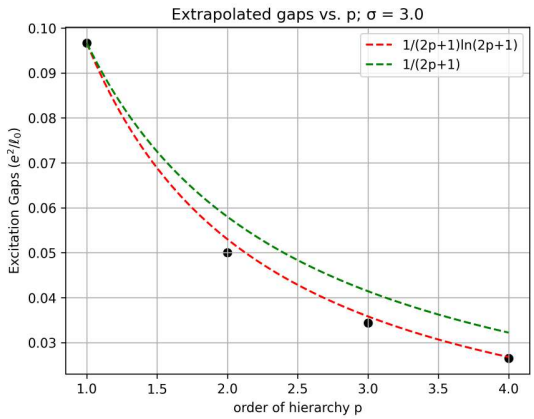

(a)

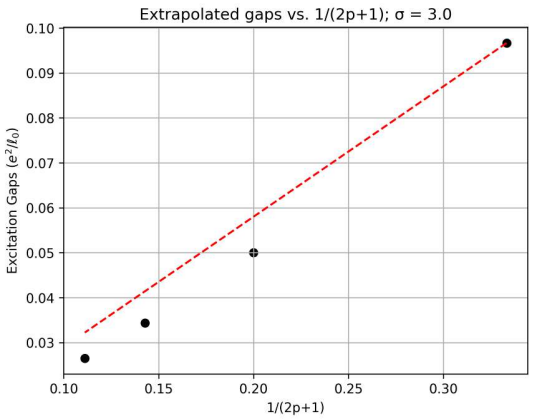

(b)

Figure 3.10: Total thermodynamic charged excitation gaps vs. order p and 1/(2p+1) for modified Gaussian interaction for $\sigma = 3.0$

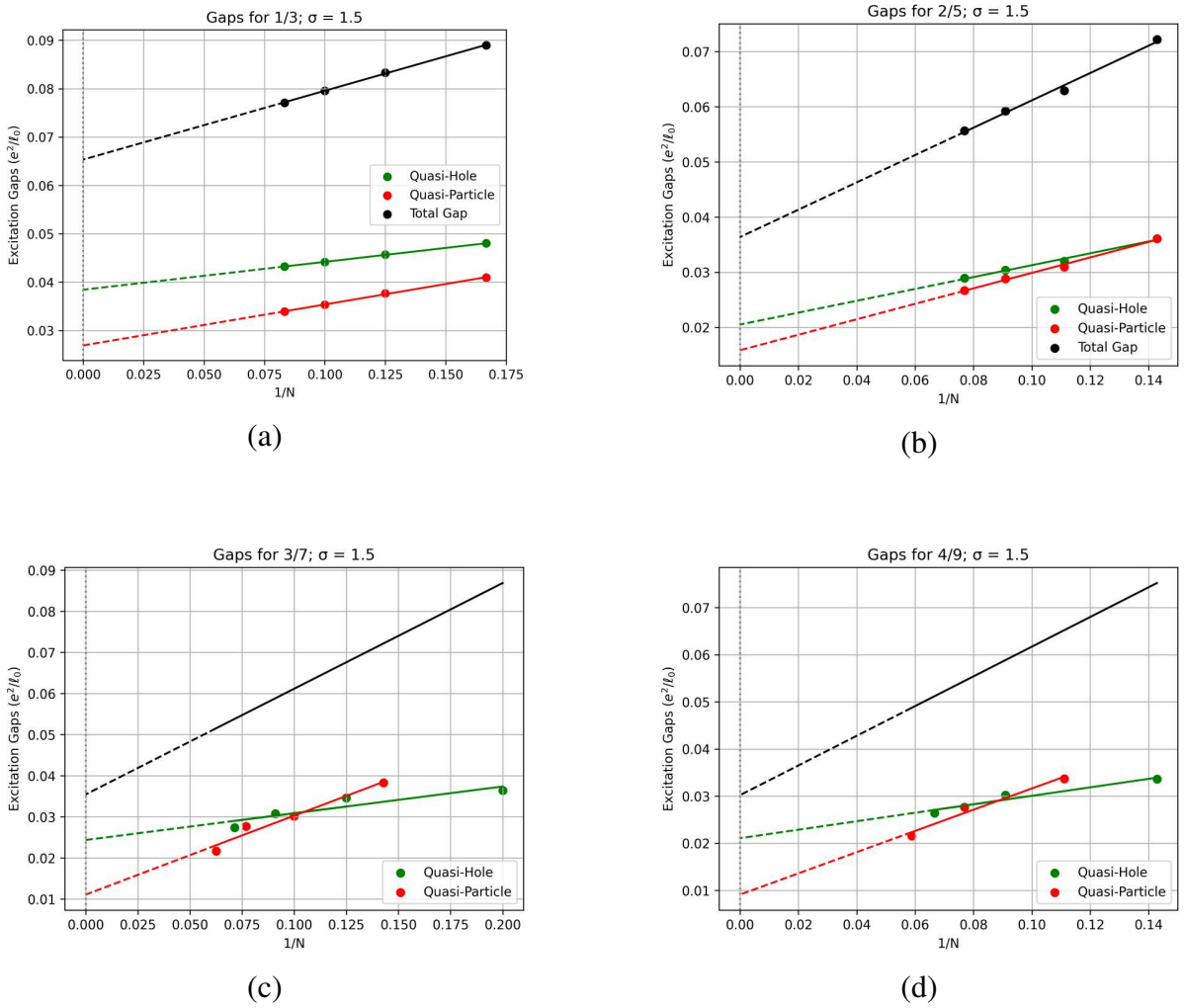

Figure 3.11: Gaps for modified Gaussian interaction $V(r) = \frac{1}{r} \cdot e^{\frac{-r^2}{2\sigma^2}}$ for $\sigma = 1.5$, extrapolated linearly to thermodynamic limit for different filling fractions.

For the modified Gaussian interaction, the thermodynamic gaps were stable for $\sigma > 1.0$, with the quasi-particle gaps becoming negative on lowering σ less than 1.0. The finite-N data showed deviations from linear scaling for small values of σ that gradually decreased, resulting in linear gap scaling for $\sigma = 3.0$ and above as shown in Fig.3.7 and Fig.3.9. The corresponding thermodynamic gaps obtained from linear extrapolation recovered the coulomb logarithmic scaling as shown in Fig.3.8 and Fig.3.10.

The results obtained so far indicate that ED on the sphere is insufficient to determine the gap scaling for short-range interactions as it is restricted to small particle numbers. Moreover, strong deviations from linearity in the finite-N data due to the geometry's curvature make thermodynamic extrapolation difficult. This motivates the need to implement tensor-network approaches like iDMRG which allows us to explore larger system sizes with cleaner scaling for finite-size effects.

On the sphere, thermodynamic limits are estimated by changing particle number N, resulting in complicated polynomial corrections to the gap energy. Furthermore, there are variations

in the observed gap scaling across different filling fractions even when the interaction is fixed. As seen in Fig.3.5, the finite-size curvature effects for short-ranged interactions are much more prominent for filling fractions 3/7 and 4/9 whereas the 1/3 and 2/5 cases effectively maintain linear scaling. When we switch to a cylinder with infinite length in the x-direction in iDMRG, the thermodynamic estimates are obtained by varying the circumference in the y-direction L_y.

A heuristic explanation for the observed trends in the finite-N data for short-ranged interactions and their deviations from the pure coulomb case is provided here, while acknowledging that this is not a complete treatment of finite-size effects on the sphere. In the thermodynamic limit, the sphere's curvature vanishes and interaction depends directly on the planar distance s separating two points on a locally flat surface as $V(s)$, whereas for the finite-N case the interaction depends on the chord length $u(s)$ connecting the points on the curved surface separated by a geodesic distance s, where $u(s) = 2R\sin\left(\frac{s}{2R}\right)$. Thus the energy obtains a correction that depends on $R \sim \sqrt{N}$. Since $s << R$ for a large sphere, the geodesic length $u(s)$ can be Taylor-expanded in powers of $1/R^2$ as

$$u(s) \approx s\left[1 - \frac{1}{6}\left(\frac{s}{2R}\right)^2 + \cdots\right] = s\left(1 - \frac{s^2}{24R^2}\right) + \mathscr{O}(R^{-4}) \tag{3.1}$$

This allows us to expand the Coulomb interaction as

$$V_C(u) \approx \frac{1}{s\left(1 - \frac{s^2}{24R^2}\right)} \approx \frac{1}{s}\left(1 + \frac{s^2}{24R^2}\right) = \frac{1}{s} + \frac{s}{24R^2}. \tag{3.2}$$

where the interaction is written as a sum of the planar $\frac{1}{s}$ contribution along with a curvature-dependent term that scales as $\frac{1}{R^2} \sim \frac{1}{N}$, resulting in the linear finite-N plots observed in Fig.3.3.

The expression for the Yukawa interaction $V_Y(u) = \frac{e^{-\kappa u}}{u}$ can be similarly expanded on substituting $u \approx s - \frac{s^3}{24R^2}$ to obtain

$$V_Y(u) \approx \frac{\exp\left[-\kappa\left(s - \frac{s^3}{24R^2}\right)\right]}{s\left(1 - \frac{s^2}{24R^2}\right)} \approx \frac{e^{-\kappa s}}{s}\left[1 + \frac{s^2}{24R^2}\right]\left[1 + \frac{\kappa s^3}{24R^2} + \frac{\kappa^2 s^6}{1152R^4} + \cdots\right]. \tag{3.3}$$

where we expand the exponent for small s as $\exp\left(\frac{\kappa s^3}{24R^2}\right) \approx 1 + \frac{\kappa s^3}{24R^2} + \frac{1}{2}\left(\frac{\kappa s^3}{24R^2}\right)^2 + \cdots$. On combining everything and grouping by powers of $\frac{1}{R^2}$, we obtain

$$V_Y(u) \approx \frac{e^{-\kappa s}}{s} + \frac{1}{R^2}\underbrace{\left[\frac{e^{-\kappa s}}{s}\left(\frac{s^2}{24} + \frac{\kappa s^3}{24}\right)\right]}_{\text{Linear Term } (1/N)} + \frac{1}{R^4}\underbrace{\left[\cdots \kappa^2 s^5 \cdots\right]}_{\text{Quadratic Term } (1/N^2)}. \tag{3.4}$$

which on integrating $V_Y(u)$ over the density profile of the excitation gives energies that scale as

$$E(N) = C_0 + \frac{C_1(\kappa)}{N} + \frac{C_2(\kappa^2)}{N^2} + \cdots \tag{3.5}$$

Unlike the case of the pure Coulomb interaction, the Yukawa case includes an additional length scale κ^{-1} that couples to the curvature. As shown in (3.4) and (3.5), κ contributes to the higher-order corrections involving powers of $\frac{1}{N}$ which were suppressed for the Coulomb case, resulting in the observed deviations from linear scaling seen in Fig.3.5. Following a similar analysis for the modified Gaussian interaction we obtain that the quadratic term $1/N^2$ is amplified by the coefficient $C_2(\frac{1}{\sigma^4})$, resulting in weaker deviations from linear scaling compared to the Yukawa case.

3.2 iDMRG on Cylinder

Following the construction outlined in section 2.5, the segment DMRG code for the excited states was implemented successfully to generate the charge-density profiles for quasi-holes and quasi-particles at filling fraction $\nu = 1/3$.

As seen in Fig.3.12 and Fig.3.13, the excitations are localized at the center of the segment with the deficit/excess in the total charge of the segment $\Delta n = n_{qh/qp} - n_{gs}$ approaching the expected values of -1/3 and +1/3 for QH and QP excitations respectively. The charge profiles for the excitations are symmetric about the center of the segment, and are in good agreement with the profiles previously obtained in literature using alternate methods such as domain-wall construction [16]. For $L_x = 12$, the segment obtains the required charge difference of $\pm 1/3$ for number of sites $L = 78$, whereas the the same charge difference is obtained at $L = 102$ for $L_x = 20$. This is consistent with the relationship between orbital spacing and the cylinder circumference $\Delta L \propto 1/L_x$. Thus, the excitation with a fixed size extends over a greater number of sites at larger values of L_x, since the orbitals are arranged closer to each other.

The gaps at finite L_x were calculated considering the Gaussian-regularized Coulomb interaction $V(r) = \frac{1}{r} e^{-r^2/2\xi^2}$ at $\nu = 1/3$, with Gaussian cutoffs $\xi = 10.0$ and $\xi = 15.0$. Extrapolation was implemented using polynomial-in-$1/L_x$ (analogous to the 1/N extrapolation in spherical ED) and exponential-in-L_x fits of the form $\Delta = \Delta_\infty + a/L_x + b/L_x^2$ and $\Delta = \Delta_\infty + Ae^{-L_x/\lambda}$ respectively. The obtained thermodynamic gaps were compared with the 1/3 gap for pure coulomb interaction $\Delta_\infty = 0.1012$ obtained from ED as reported in [4]. As seen Fig.3.14 (a), the polynomial fit for $\xi = 10.0$ does not converge monotonically towards the extrapolated value as $1/L_x \to 0$, with pronounced curvature near the extrapolation limit. On the other hand, the exponential fit is well-behaved for both $\xi = 10.0$ and $\xi = 15.0$, with corresponding thermodynamic gaps $\Delta_\infty = 0.0998$ and $\Delta_\infty = 0.1006$. The relative errors for these two estimates with respect to the expected value ($\sim 1.4\%$ and $\sim 0.6\%$ respectively) indicate that the values converge to the expected gap as the interaction approaches the pure coulomb case.

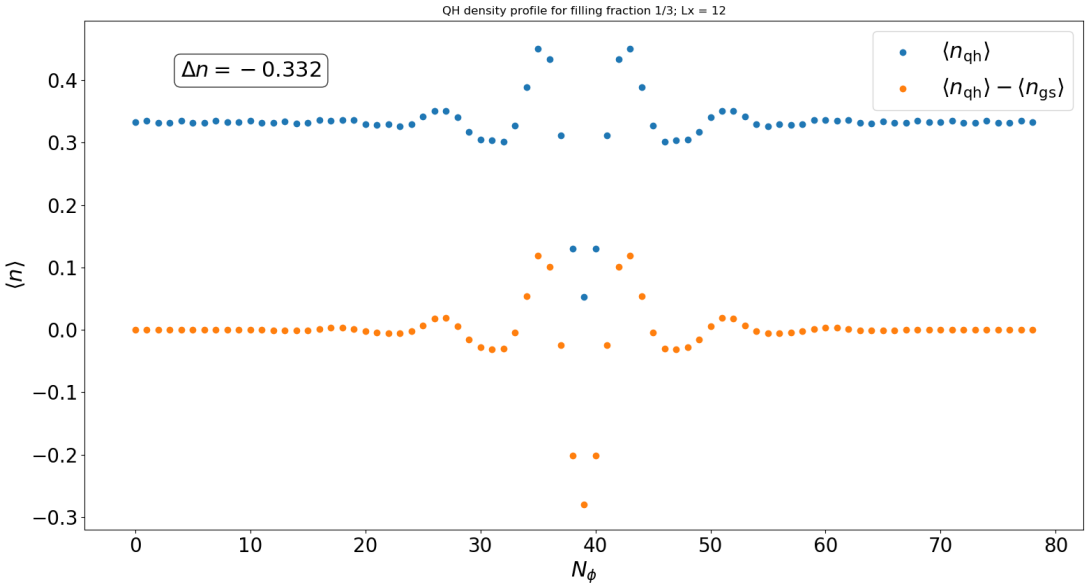

(a)

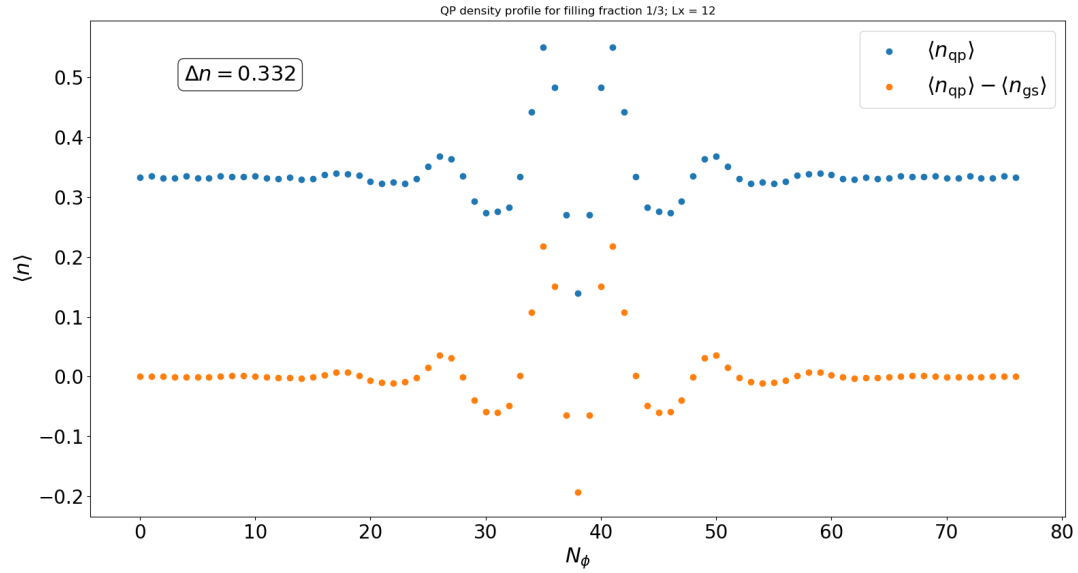

(b)

Figure 3.12: Charge density profile for quasi-hole (a) and quasi-particle (b) excitations for circumference $L_x = 12$; segment length $L = 78$.

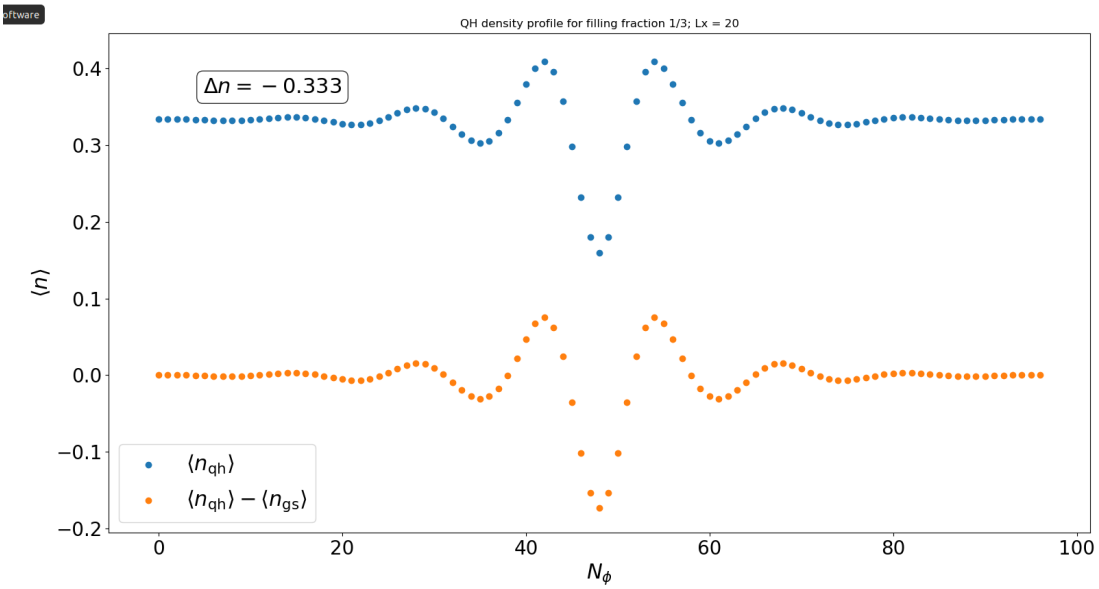

(a)

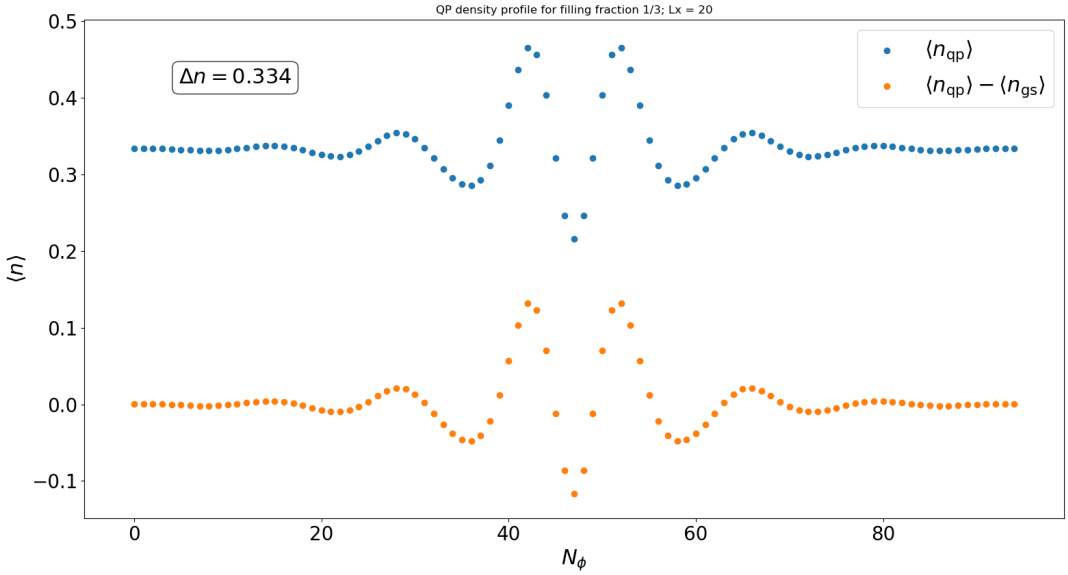

(b)

Figure 3.13: Charge density profile for quasi-hole (a) and quasi-particle (b) excitations for circumference $L_x = 20$; segment length $L = 102$.

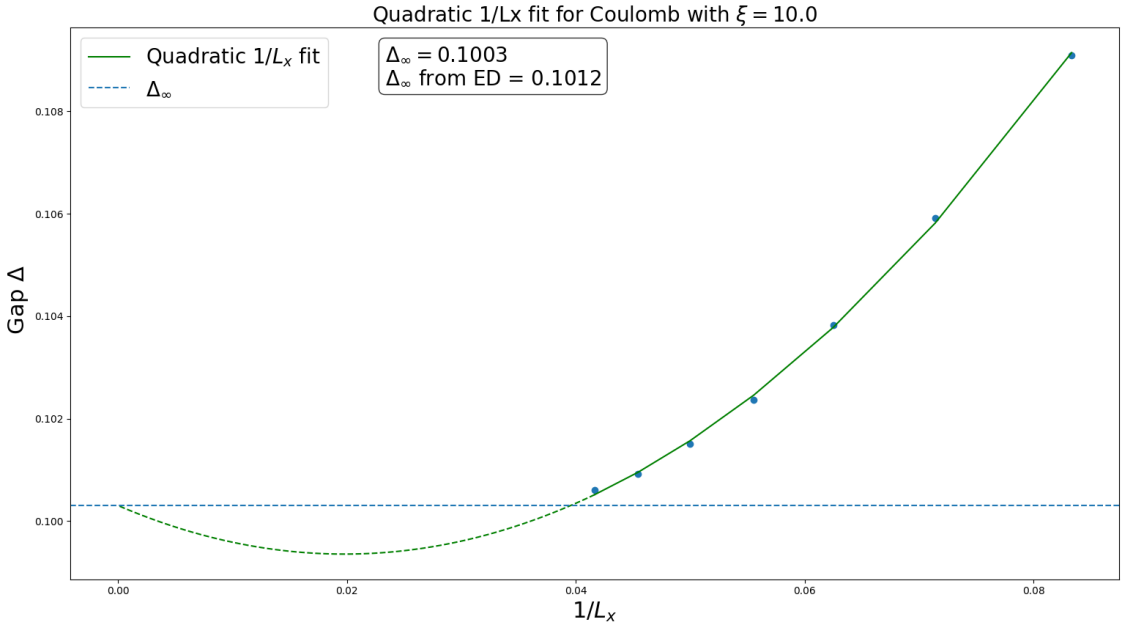

(a)

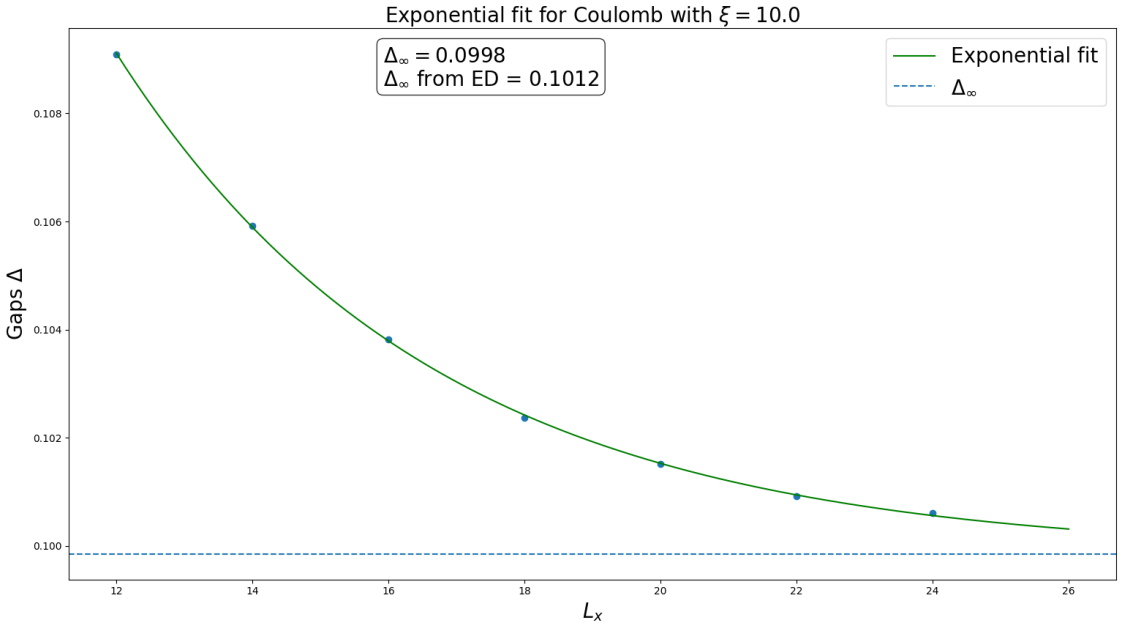

(b)

Figure 3.14: Excitation gaps for coulomb interaction with Gaussian cutoff $\xi = 10.0$ at $\nu = 1/3$ extrapolated to the thermodynamic limit ($L_x \to \infty$) using (a) Quadratic in $1/L_x$ and (b) Exponential in L_x fits

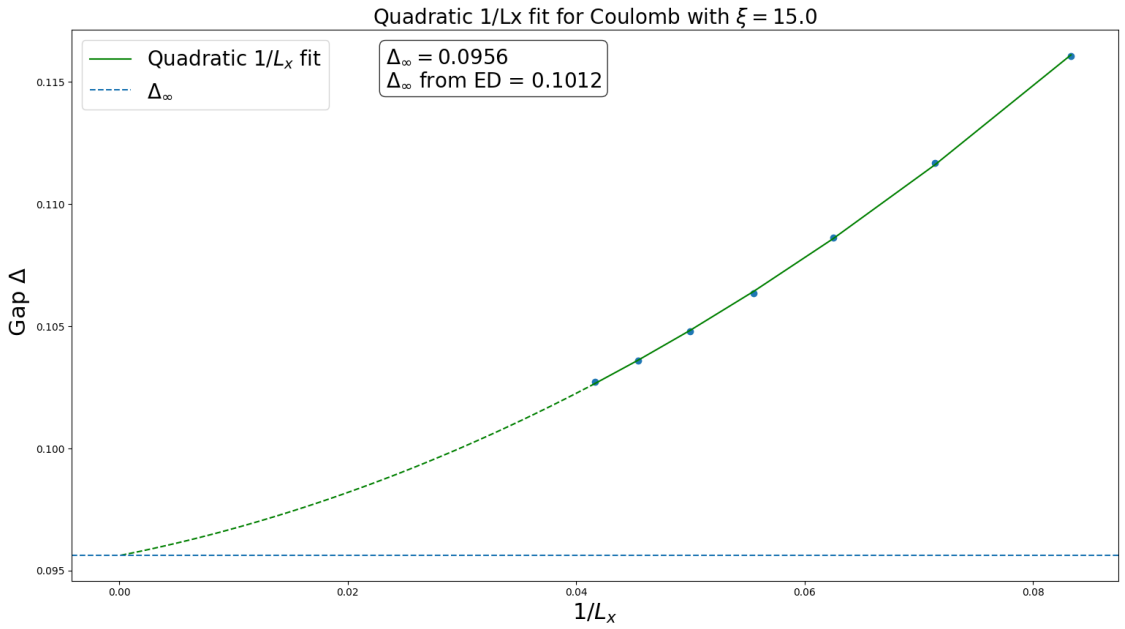

(a)

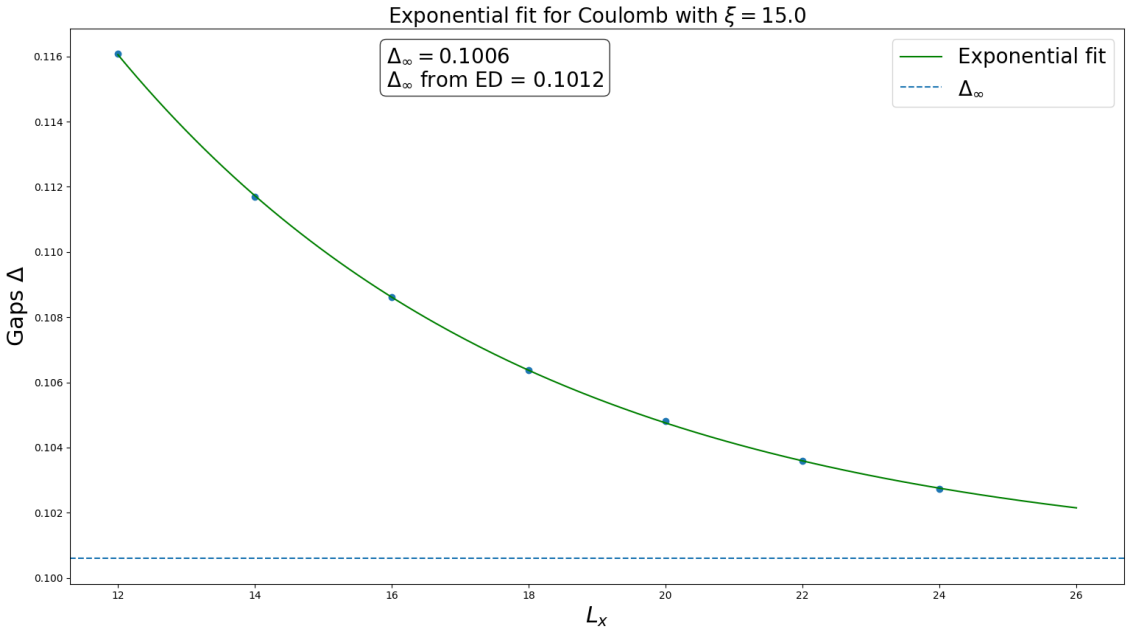

(b)

Figure 3.15: Excitation gaps for coulomb interaction with Gaussian cutoff $\xi = 15.0$ at $\nu = 1/3$ extrapolated to the thermodynamic limit ($L_x \to \infty$) using (a) Quadratic in $1/L_x$ and (b) Exponential in L_x fits

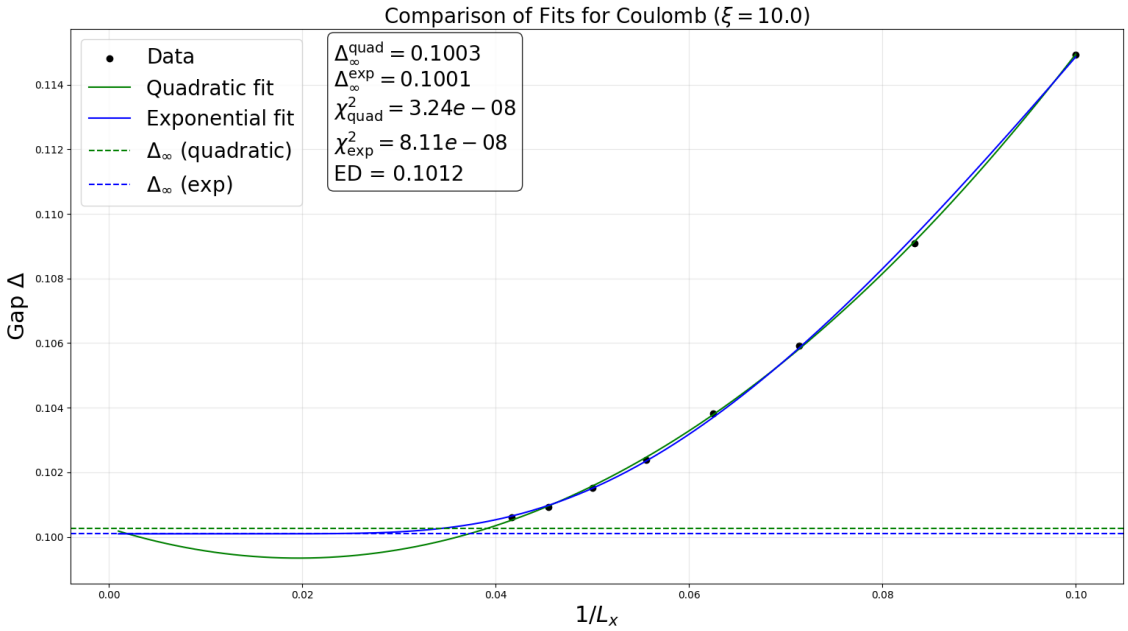

(a)

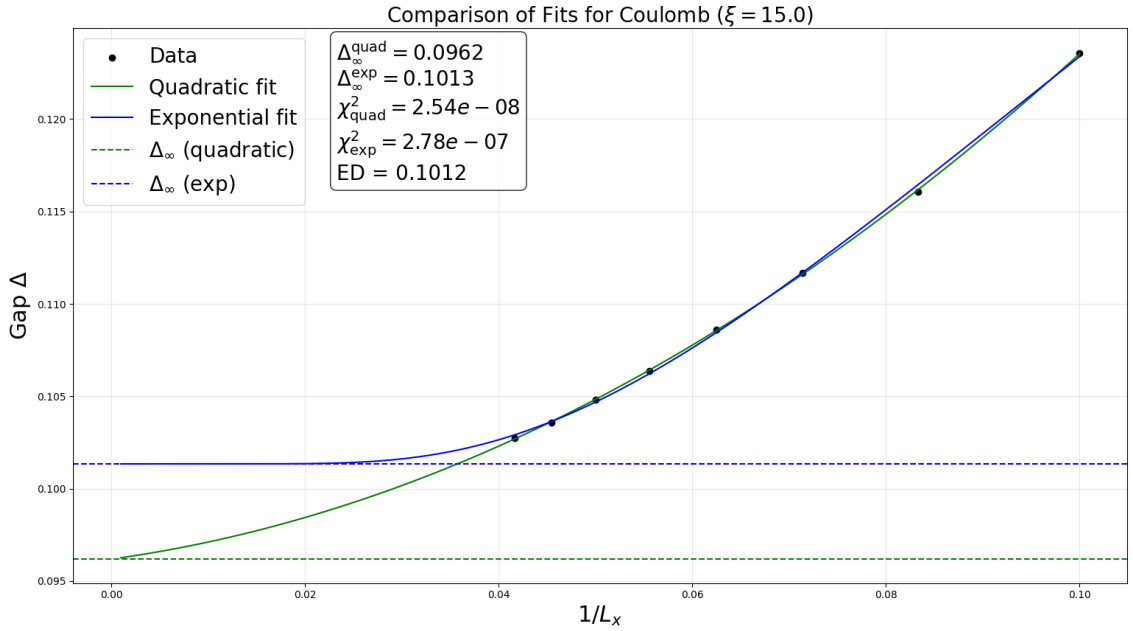

(b)

Figure 3.16: Excitation gaps for coulomb interaction with Gaussian cutoff $\xi = 10.0$ and 15.0, with both exponential L_x and quadratic $1/L_x$ fits plotted against $1/L_x$. The thermodynamic extrapolate from the exponential converges to the expected gap value $\Delta_\infty = 0.1012$ as the cutoff is increased, although the quadratic fit yields a lower χ^2 value in both cases.

Chapter 4

Summary and Conclusions

The primary objective of this work was to compute the charged excitation gaps for Jain states $p/2p+1$ approaching half-filling, and to extrapolate the obtained results to the thermodynamic limit. This was aimed at uncovering any changes in the scaling of the thermodynamic gaps as the interaction was varied from coulomb to short-ranged. The motivation for this study stems from the association of the gap scaling at half-filling with the effective mass $m^*(p)$, thus offering an indirect way to probe the underlying composite-fermion physics.

Exact Diagonalization was performed for systems of up to 17 particles on the Haldane sphere. The resulting finite-size data was extrapolated to the thermodynamic limit, yielding coulomb gap values in good agreement with those reported in literature, including their scaling with Jain index p [4]. The gaps were calculated after carefully accounting for background corrections and interpolating/extrapolating the energy values between the available system sizes. However, the presence of strong finite-size effects, along with access to limited system sizes prevented the reliable extrapolation of gaps for short-ranged interactions. These limitations prompted the transition to infinite DMRG on a cylinder, which allows access to larger effective system sizes.

The ground state, quasi-hole and quasi-particle energies for gap calculation were obtained using a segment DMRG approach, wherein a finite segment of suitable length was embedded between left and right environments obtained from a converged infinite ground state, allowing us to localize the excitation in an otherwise infinite system. The thermodynamic gaps were estimated by extrapolating the gaps obtained for different values of the cylinder circumference L_x, where the considered values of L_x ranged from 12 to 24 l_b. The thermodynamic gap for the coulomb interaction at filling fraction 1/3 was obtained by extrapolating the finite-size data with exponential fit in L_x. The resulting gap was found to match the expected value. However, the estimates obtained from the polynomial fit in $1/L_x$, analogous to the extrapolation for finite-size data as previously implemented on the sphere [4] and finite-length cylinders [23], was found to slightly underestimate the gap in the thermodynamic limit. This is suggestive of a qualitative difference between finite-system scaling on a sphere/finite cylinder and the infinite cylinder, with exponential scaling providing a more appropriate description in the present case.

Future work will involve the use of high-performance computing clusters to obtain the thermodynamic gaps for higher filling fractions along the Jain sequence with the aim of obtaining the corresponding gap scaling.

Bibliography

[1] David Tong. Lectures on the quantum hall effect. *arXiv preprint arXiv:1606.06687*, 2016.

[2] Robert B Laughlin. Anomalous quantum hall effect: An incompressible quantum fluid with fractionally charged excitations. *Physical Review Letters*, 50(18):1395, 1983.

[3] F Duncan M Haldane and Edward H Rezayi. Finite-size studies of the incompressible state of the fractionally quantized hall effect and its excitations. *Physical review letters*, 54(3):237, 1985.

[4] RH Morf, N d'Ambrumenil, and S Das Sarma. Excitation gaps in fractional quantum hall states: An exact diagonalization study. *Physical Review B*, 66(7):075408, 2002.

[5] Jainendra K. Jain. *Composite Fermions*. Cambridge University Press, 2007.

[6] Kalin Vetsigian. Chern-simons theory of the fractional quantum hall effect. `https://guava.physics.ucsd.edu/~nigel/Courses/Web%20page%20569/Essays_2002/files/vetsigian.pdf`, 2001. Unpublished manuscript / lecture notes.

[7] Bertrand I Halperin, Patrick A Lee, and Nicholas Read. Theory of the half-filled landau level. *Physical Review B*, 47(12):7312, 1993.

[8] F Duncan M Haldane. Fractional quantization of the hall effect: A hierarchy of incompressible quantum fluid states. *Physical Review Letters*, 51(7):605, 1983.

[9] Michael Arciniaga and Michael R. Peterson. Landau level quantization for massless dirac fermions in the spherical geometry: Graphene fractional quantum hall effect on the haldane sphere. *Phys. Rev. B*, 94:035105, Jul 2016.

[10] Rachel Elizabeth Wooten. *Haldane pseudopotentials and Landau level mixing in the quantum Hall effect*. Phd dissertation, University of Tennessee, 2013.

[11] A. R. Edmonds. *Angular Momentum in Quantum Mechanics*. Princeton University Press, 1957.

[12] Tai Tsun Wu and Chen Ning Yang. Some properties of monopole harmonics. *Physical Review D*, 16:1018–1021, 1977.

[13] DiagHam. https://www.nick-ux.org/diagham.

[14] R. Morf, N. d'Ambrumenil, and B. I. Halperin. Microscopic wave functions for the fractional quantized hall states at $\nu = \frac{2}{5}$and$\frac{2}{7}$. *Phys. Rev. B*, 34:3037–3040, Aug 1986.

[15] Ajit C Balram, Anirban Sharma, and JK Jain. Interplay of superconducting, metallic, and crystalline states of composite fermions at ν= 1 6 in wide quantum wells. *Physical Review B*, 112(3):035118, 2025.

[16] Michael P Zaletel, Roger SK Mong, and Frank Pollmann. Topological characterization of fractional quantum hall ground states from¡? format?¿ microscopic hamiltonians. *Physical review letters*, 110(23):236801, 2013.

[17] Zi-Xiang Hu, Z. Papić, S. Johri, R.N. Bhatt, and Peter Schmitteckert. Comparison of the density-matrix renormalization group method applied to fractional quantum hall systems in different geometries. *Physics Letters A*, 376(30):2157–2161, 2012.

[18] Grégoire Misguich and Th Jolicoeur. Dmrg study of fqhe systems in the open cylinder geometry. In *Journal of Physics: Conference Series*, volume 1740, page 012043. IOP Publishing, 2021.

[19] Johannes Hauschild and Frank Pollmann. Efficient numerical simulations with tensor networks: Tensor network python (tenpy). *SciPost Physics Lecture Notes*, page 005, 2018.

[20] Ulrich Schollwöck. The density-matrix renormalization group in the age of matrix product states. *Annals of physics*, 326(1):96–192, 2011.

[21] Jens Eisert, Marcus Cramer, and Martin B Plenio. Colloquium: Area laws for the entanglement entropy. *Reviews of modern physics*, 82(1):277–306, 2010.

[22] JK Jain and RK Kamilla. Composite fermions in the hilbert space of the lowest electronic landau level. *International Journal of Modern Physics B*, 11(22):2621–2660, 1997.

[23] AE Feiguin, E Rezayi, C Nayak, and S Das Sarma. Density matrix renormalization group study of incompressible fractional quantum hall states. *Physical review letters*, 100(16):166803, 2008.